SURFACE PLASMON RESONANCE FOR SENSING PHASE CHANGES IN OPAQUE MATERIALS

by

Raha Khosravi

Submitted in partial fulfillment of the requirements
for the degree of Master of Applied Science

at

Dalhousie University
Halifax, Nova Scotia
December 2020

This thesis is dedicated to Yashar, for his kindness and devotion, and for his endless support when I was working on my projects!

Table of contents

List of Tables

List of Figures

Abstract

The accurate and real-time detection of phase changes of opaque materials during different physical, chemical and mechanical processes is relevant in various industrial applications. In this dissertation, detection and monitoring of refractive index variations of opaque materials during phased changes using prism-based surface plasmon resonance (SPR) sensors have been reported. Using the Kretschmann configuration of SPR, a sensitive refractive index sensor has been designed which can relate the SPR absorption peak wavelength of the sensor to the sample refractive index. In particular, the phase changes of asphaltene in crude oil during its deposition, the role of inhibitors on the deposition rate and depth of asphaltene, and also the phase change of resin composite during curing process via UV light in dental applications have been studied. Using our SPR sensor for crude oil depositions, we can detect 142 nm SPR peak shift from 553± 0.6 nm to 695±0.6 nm, for a 0.197 change in refractive index (RI) from 1.389 to 1.586. This is used to show crude oil RI varies from a RI value of 1.505 (SPR peak wavelength of 601 nm) in neat crude oil fluid to a RI value of 1.521 (SPR peak wavelength of 614 nm) when asphaltenes deposited on the surface of the sensor completely. In dental application, we similarly show that resin composite SPR peak wavelength shifts from 617±0.6 nm before UV curing to 633±0.6 nm after a complete UV curing. Furthermore, we used the matrix formalization modelling approach for calculating the theoretical SPR response from our sensor and it was in excellent agreement with our observed experimental results. Our findings show the potential of SPR sensors in various industrial and scientific applications, in particular applications in dentistry and oil industries for online real-time monitoring.

Acknowledgements

I would like to express my deepest appreciation to my supervisor Dr. Vincent Sieben for his excellent scientific guidance, continuous support and motivation during my M.Sc. program. I would also like to thank my committee members, Dr. Sergey Ponomarenko and Dr. Adam Donaldson for their support and recommendations.

Chapter 1

Introduction

1.1 Thesis theme

Optical technologies have been used in different aspects of human life including communications [1], medical therapies [2] and sensing [3,4]. Between different applications of optics, optical sensing applications are among the most accurate ones as they allow scientists and engineers to measure different properties of materials including their refractive index, temperature and pressure [5]. Optical sensors allow label-free detection and monitoring of different materials in real-time and with a low cost which make them attractive devices for application in medicine [6–8], dentistry [9, 10], oil industry [11, 12] and environmental monitoring [13]. In particular, the real-time detection of phase changes of asphaltene in crude oil during deposition in pipelines, and resin composite during curation in dental applications are fundamentally important to the researchers in the fields of oil [11, 12] and dentistry [8]. In this thesis, we focus on detection and monitoring the opaque materials and their phase changes using surface plasmon resonance sensors as a novel optical sensing technology. This chapter starts with an introduction to general theme of this dissertation, followed by the objectives of the thesis and then the thesis organization is presented.

1.2 Thesis objectives

This thesis will contribute to our understanding of the SPR sensors and their application in various sectors such as dentistry and oil industry. The goals of this thesis are:

- Provide a summary of conventional and state-of-the-art methods for refractive index detection in opaque materials.

- Provide background information on surface plasmon resonance, different type of surface plasmon resonance sensors and their application in refractive index sensing.

- Developing a theoretical framework to study prism-based surface plasmon resonance sensors for refractive index detection of opaque materials.

- Design of surface plasmon resonance sensor for detection of phase changes of asphaltene in crude oil during deposition.

- Design of surface plasmon resonance sensor for detection of phase changes of resin composite after curing with UV light in dental applications.

1.3 Thesis organization

This dissertation is composed of a brief introduction to the physical concepts of the theories used throughout the thesis along with the results of our research as a published journal paper and another paper which is in-progress.

Chapter 2 briefly reviews the concept of opaque materials, refractive index and different methods of refractive index measurements in opaque materials including spectroscopic ellipsometry, Fourier transform infrared (FTIR) spectroscopy and surface plasmon resonance.

Chapter 3 discusses background theory on the physics of surface plasmon resonance (SPR). In this chapter, the importance of the study of SPR resonance is further investigated and then different type of SPR sensors as well as different interrogation methods will be studied in detail.

Chapter 4 describes the theoretical framework of the prism-based SPR sensors as a layered media using matrix method. In this chapter, the theoretical model is developed and then the model has been applied to a particular case of asphaltene deposition in crude oil to predict the output absorbance spectra of the SPR sensor.

Chapter 5 presents the data analysis process of the SPR sensor. In this chapter, we described the SPR sensor components in detail and showed how we can obtain absorbance spectra of the opaque materials using the output intensities of the SPR sensor. The customized LabView program which has been used to detect and visualize the absorption spectra and SPR peak wavelength has been also explained in detail. We also described the calibration process of the SPR sensor and obtained the relationship between SPR peak wavelength and sample refractive index. Finally, this chapter briefly examines the reproducibility and reliability of the results and the role of signal noise in experiments.

Chapter 6 investigates the application of SPR sensor in oil industry. In particular, we used a SPR sensor for monitoring asphaltene deposition in crude oil and demonstrated the effects of inhibitors on asphaltene deposition. We show that crude oil RI varies from a RI value of 1.505 (SPR peak wavelength of 601 nm) in neat crude oil fluid to a RI value of 1.521 (SPR peak wavelength of 614 nm) when asphaltenes deposited on the surface of the sensor completely.

Chapter 7 presents the study of resin composite curing in dentistry and its phase changes during UV irradiation using SPR sensor. We show how the illumination time

and distance can affect resin refractive index during the curing process. Furthermore, we show that resin composite SPR peak wavelength shifts from 617 nm before UV curing to 633 nm after a complete UV curing.

Chapter 8 provides a brief summary of the main results of this thesis along with suggestions for future work.

1.4 Research output

The following journal article and conference proceedings are published based on this thesis:

Journal paper:

R. Khosravi, C. Rodriguez, F. Mostowfi, V. Sieben "Evaluation of crude oil asphaltene deposition inhibitors by surface plasmon resonance,", Fuel273, 117787 (2020). https://doi.org/10.1016/j.fuel.2020.117787

Conference proceedings:

R. Khosravi, C. Rodriguez, V. Sieben "Studying asphaltene deposition inhibitors using surface plasmon resonance,"Photonics North 2020, Niagara Falls,ON, Canada (2020).

R. Khosravi, F. Che, Ch. Felix, M. Hajati, S. Ponomarenko, V. Sieben, "Novel plasmonic sensor for real-time monitoring of resin cure,"International association for dental research (IADR), Washington, D.C, USA (accepted but the conference delayed due to COVID-19).

Chapter 2

Refractive index sensing in opaque materials

During the last few years, the measurement of the refractive index (RI) of materials has been the focus of intense research [14]. RI detection is broadly investigated in different areas such as chemistry and biological sciences as it enables label-free sensing [14, 15]. With label-free detection one can detect a sample without adding external markers and affecting the intrinsic characteristics of the sample [16]. Furthermore, with the advance of optical sources and detectors, methods which allow remote and contact-less analyses have been taken into practice which enables minimally invasive detection [14–16]. This chapter will provide a brief introduction to different types of materials (particularly, opaque materials), refractive index, and different state-of-the-art RI sensing methods.

2.1 Opaque materials

Based on the light transmission/reflection properties, materials can be divided into three main categorizes: transparent, translucent and opaque (Fig. 2.1). When light encounters transparent materials, most of it passes directly through them [17]. As an example, glass (silica) is transparent to visible light (400-700 nm) meaning it allow most of the visible light to pass through it. This is why we can clearly see through the glass. When light encounters translucent materials, a portion of the light passes through them. The transmitted light will change its direction many

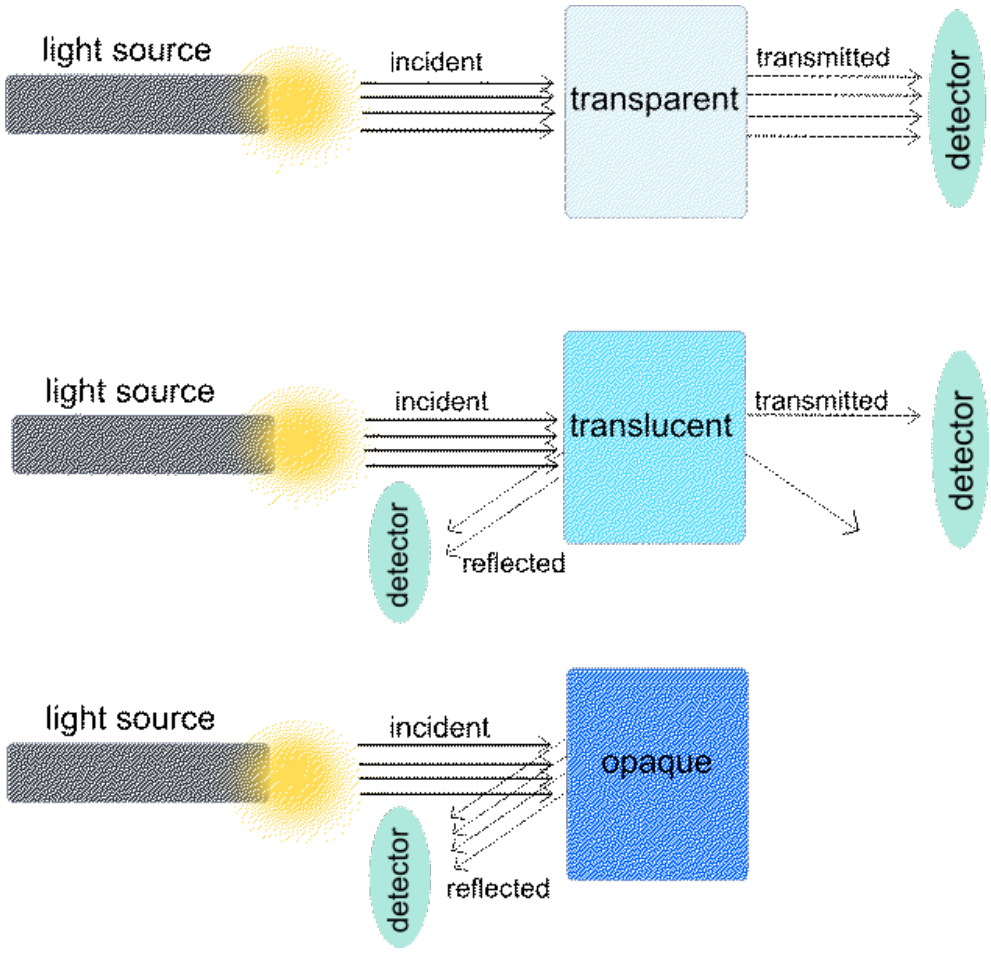

Figure 2.1: Three main categories of materials based on their light transmission/reflection properties: transparent (top), translucent (middle) and opaque (bottom).

times and will be scattered as it passes through a translucent material [17]. As a result, one cannot see clearly through translucent materials and the objects on the other side of a them appear unclear [18]. The last category of materials are opaque materials which encompass most of the materials in nature. When a light beam encounter with an opaque material, the majority of the light rays cannot passes through the object. Therefore, most of the light rays are either reflected by the object or absorbed and converted to heat or thermal energy [17–19]. Light attenuation in opaque materials happens due to scattering effects (e.g. Rayleigh) and absorbance

(molecular). Materials such as asphaltene in crude oil, dental resin composite, and most of the metals are opaque to visible light. The color of an opaque material is then related to the wavelengths of the light which has been reflected the most from the object [18,19]. As measuring the light transmission through opaque objects is difficult, the light reflectance measurements are typically used to optically characterize opaque materials.

2.2 Refractive index

Refractive index (RI), which sometimes also called index of refraction, is a parameter that describes how fast light travels through the material comparing to the vacuum [20]. According to this definition, RI (n) is equal to the velocity of light c for a given wavelength in vacuum divided by its velocity v in a substance $n = \frac{c}{v}$. The familiar Snell's law uses the RI of two materials at an interface to describe the bending of a light ray when it is passes from one medium into a second medium Fig. 2.2. . If i is the incidence angle (angle between the incoming ray in vacuum and the normal to the surface) and r is the refraction angle (the angle between the ray in the medium and the normal), the refractive index n is defined as the ratio of the sine of the incidence angle to the sine of the refraction angle $n = \frac{\sin(i)}{\sin(r)}$ [20] . RI is an important parameter which can describe physical and chemical properties and also the state of a given substance [21] . Therefore, detection of RI for an opaque material is particular interest for scientists in different fields such as chemistry, physics, medical sciences and biology [20, 21]. In the next sections, different state-of-the-art methods for detection of RI of materials will be discussed briefly.

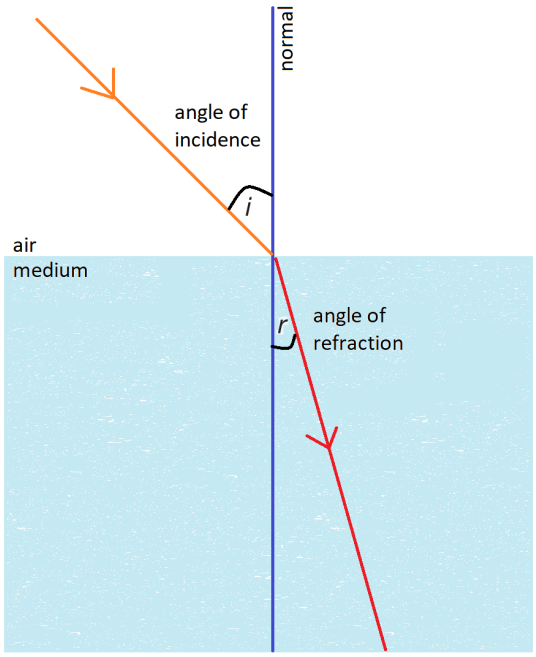

Figure 2.2: Schematic of a refraction of a light ray at the interface between two medium which can be characterized by refractive index.

2.3 Complex refractive index and permittivity

When a light beam propagates through a material, some part of the light will always be attenuated [22]. The light attenuation during propagation in a medium can be taken into account by defining a complex refractive index [22, 23], where $n(\lambda)$ is the real index of refraction and $k(\lambda)$ is the index of absorption or imaginary part of the complex refractive index [22].

$$\bar{n}(\lambda) = n(\lambda) + ik(\lambda) \tag{2.1}$$

name of material	n@$\lambda = 500$nm	k@$\lambda = 500$nm	n@$\lambda = 600$nm	k@$\lambda = 600$nm
Air	1.00027897	0	1.00027698	0
Silver	0.050000	3.1309	0.055159	4.0097
Benzene	1.5053	0	1.4948	0
Heptane	1.3927	0	1.3885	0
Gold	0.97112	1.8737	0.24873	3.074
Toluene	1.5057	1.3886e-8	1.4958	1.3560e-8

Table 2.1: Refractive index of selected materials (n=real part and k=imaginary part)

The index of absorption is also called the absorption constant, index of extinction, or extinction coefficient of the material. Table 2.1, shows the complex refractive index (RI) of some materials in different wavelengths [22]. It should be noted that complex refractive index is a wavelength dependent parameter. For example, it can be seen that RI of toluene decreases from 1.5057 at 500 nm to 1.4958 at 600 nm. Another example is the RI of glass and sapphire which decreases from 1.524 and 1.7742 at 500 nm to 1.5163 and 1.7675 at 600 nm, respectively. It should also be noted that imaginary part of RI which indicate optical losses can be significant for metals like gold and silver at optical frequencies (visible and near infrared) while it can be negligible for some other materials like glass. The same wavelength dependent trend is also exist for imaginary part of RI of materials. For example, gold imaginary part of RI (k) increases from 1.8737 at 500 nm to 3.0740 at 600 nm. The complex RI is derived from the permittivity and permeability of a material, when describing electromagnetic wave propagation within and across various media using Maxwell's equations. Permittivity describes the polarizability of the material in response to an applied electric field [23]. Like RI, permittivity depends on the wavelength and can be a complex value consist of real and imaginary parts. For a given material, complex refractive index $\bar{n}(\lambda)$ and complex permittivity $\epsilon(\lambda)$ are related through the following formulas [23], where $\epsilon'(\lambda)$ is the real part of the permittivity and $\epsilon''(\lambda)$ is

the imaginary part of the complex permittivity.

$$\begin{aligned} \bar{n}(\lambda) = n(\lambda) + ik(\lambda) = \sqrt{\epsilon(\lambda)} = \sqrt{\epsilon'(\lambda) + i\epsilon''(\lambda)} \\ \epsilon'(\lambda) = n^2(\lambda) - k^2(\lambda) \\ \epsilon''(\lambda) = 2n(\lambda)k(\lambda) \\ n^2(\lambda) = \frac{1}{2}[\epsilon'(\lambda) + \sqrt{\epsilon'^2(\lambda) + \epsilon''^2(\lambda)}] \\ k^2(\lambda) = \frac{1}{2}[-\epsilon'(\lambda) + \sqrt{\epsilon'^2(\lambda) + \epsilon''^2(\lambda)}] \end{aligned} \tag{2.2}$$

It should be noted that Equation 2.2 assumes that the materials under study are non-magnetic materials with a relative permeability (μ_r) of 1. The complex RI or permittivity of a material cannot be directly measured. Therefore, there are indirect methods to measure complex RI of materials which will be described in the following section.

2.4 Refractive index sensing methods

2.4.1 Refractive index sensing using ellipsometry

Ellipsometry is an optical measurement technique that can be used to detect opaque materials using the light reflection (or transmission) from samples [24]. The main mechanism of detection in ellipsometry is that it measures the change in polarized light upon light reflection on a material surface [25]. As the polarized reflected light often becomes elliptical upon light reflection, this technique is called 'ellipsometry'. Ellipsometry is based on measuring the two important parameters (ψ, Δ) which represent the amplitude ratio and phase difference between light polarization states known as p and s-polarized light waves [24, 25]. In spectroscopic ellipsometry (ψ, Δ) spectra are measured by changing the wavelength of input light against the sample. In

general, the spectroscopic ellipsometry measurements are usually performed in the ultraviolet/visible (UV-Vis) region, but measurement in the infrared region is also possible. For detection using ellipsometry, we usually need a thin film of the sample to be able to perform measurements [26]. Spectroscopic ellipsometry has a lot of different application in different fields [24]. Interestingly, not only characterization of thin films but also process diagnoses including etching and thermal oxidation can be measured using ellipsometry technique. As the light can be used to detect

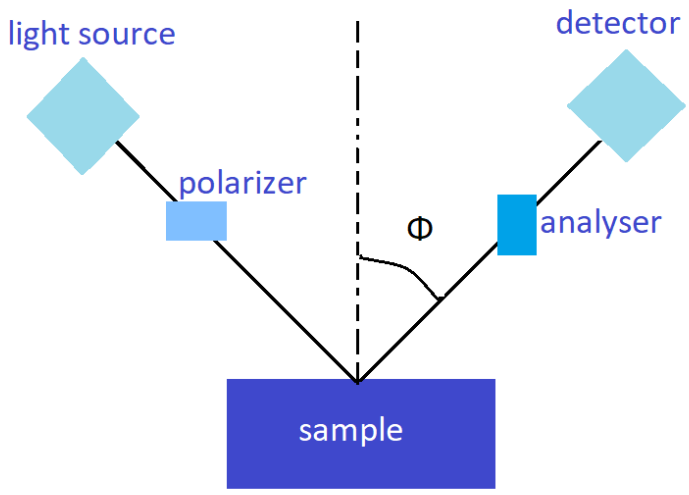

Figure 2.3: Schematic of ellipsometry measurements for detection of sample on thin films.

the sample, spectroscopic ellipsometry allows characterization of thin films formed in solutions which can be of special interest to scientists in the field of chemistry and biology [25,26]. There are two general restrictions for the ellipsometry technique: (1) surface roughness of the films should be small (smooth films are required), and (2) the measurement must happen at oblique incidence. The main reason for these limiations is that the surface roughness signifcantly reduces the reflected light intensity. As ellipsometry determines a polarization state from its light intensity, ellipsometry

measurement for non-smooth films becomes inefficient and difficult [24].

2.4.2 Refractive index sensing using FTIR method

Fourier transform infrared (FTIR) spectroscopy is a vibrational spectroscopic technique which can be optically detect the molecular changes in materials and samples [27]. FTIR utilizes an instrument which can obtain the absorption spectrum of a given material which is called spectrometer. Fig. 2.4 schematically illustrates

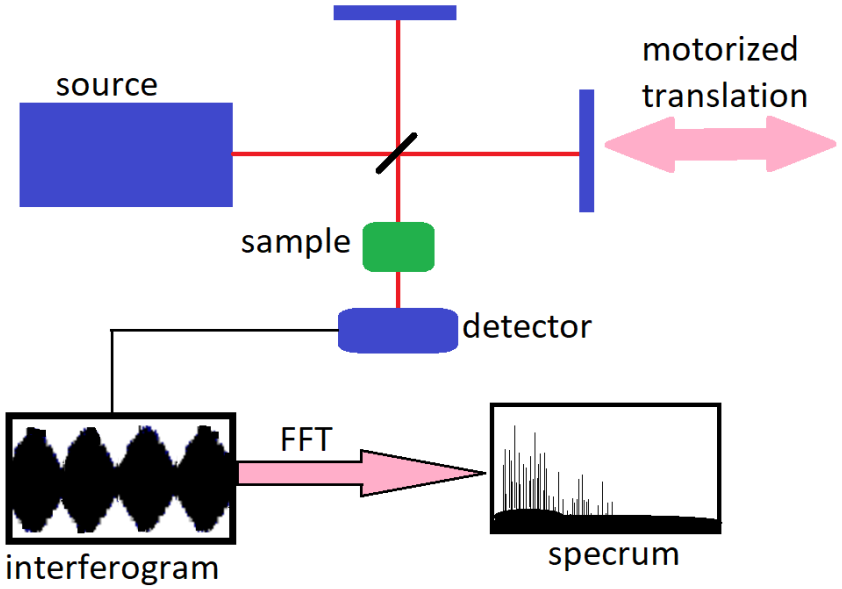

Figure 2.4: Schematic demonstration of the main component of a simple FTIR spectrometer.

the main component of a simple FTIR spectrometer. The instrument produces an IR light beam, which is passes through the interferometer where the spectral encoding happens [27]. Interferometer is then recombine the light beams which have different in-path lengths. This will create constructive and destructive interferences which is called interferogram [27, 28]. Then, the beam enters into the sample position

and the sample absorbs specific frequencies of the IR light energy. The absorption spectrum generated in interferogram is unique to each material. Next, the optical detector receive and detect the interferogram signal (spectra) while another beam is superimposed to provide a reference for the instrument operations [29]. Finally, the final sample (material) spectrum can be obtained after the interferogram spectra subtracted from the spectrum of the background by Fourier transformation computer software [29]. FTIR spectrometers are usually utilized for measurements in the middle-IR (mid-IR) 3-15 µm and near-IR 0.75-3 µm regions [28]. As the Fourier transform (FT) spectrometer provides the near-IR and mid-IR spectrum much faster compared to the conventional spectrometer, FTIR spectroscopy is one of the state-of-the-art methods in detecting unknown substances in different areas of science [29]. In addition to conventional FTIR, attenuated total reflectance (ATR) is another technique which can be used with FTIR spectrometers [30]. The ATR-FTIR technique is based on a reflectance measurements in contrast to conventional FTIR which is based on tranmission of IR light [30]. The ATR-FTIR technique makes it possible to study of materials which are highly absorptive in the IR region [30]. Using ATR-FTIR, one can study optical properties of opaque materials such as RI and permittivty as ATR-FTIR does not depend on the transmitted light from the material.

2.4.3 Refractive index sensing using surface plasmon resonance

RI sensing based on surface plasmon resonance (SPR) is one of the main methods in detection of unknown materials and in particular, opaque materials [31]. SPR sensors detect the absorption of light energy due to interaction of light beams and surface electrons at the interface between a metal and dielectric due to small changes in RI of the material at the sensing interface [32]. SPR-based RI sensors have important applications in areas like chemistry, biology, medical sciences and oil industry [11,

31]. For example, SPR sensors have been used for gas sensing [33], detection of various biomolecules including proteins, nucleic acids, and viruses [34], and analyze developments or chemical interactions in live cells [34]. Table below is a comparison of these three techniques.In the next chapter, the basics of surface plasmon resonance, different types of SPR sensors and different SPR interrogation methods will be studied in detail.

name of the techniques	SPR	FTIR	Ellipsometry
operation wavelength	UV-visible	near IR-mid IR	UV-visible-near IR
cost	$\sim$ 30K	$\sim$ 100k	$\sim$ 40k
published articles (2010-2021)	31,959	204,104	10,431

Table 2.2: Comparison of FTIR, SPR and Ellipsometry techniques. Please note that the data are acquired in November 10, 2020 from Science Direct (https://www.sciencedirect.com) using the following keywords: FTIR, SPR and ellipsometry.

Chapter 3

Surface plasmon resonance sensors

3.1 Principles

Pines and Bohm had suggested in the 1950s that energetic electrons which passes through metallic foils can experience characteristic energy loss due to the excitation of plasmons [35]. Then, Thurbadar observed a large drop in reflectivity when illuminating thin metal films on a substrate [36]. In 1960s and 1970s many scientists including Otto and Kretschmann worked on explaining Thurbadar's results [36]. Otto for example showed that the drop in the reflectivity in the previous experiments is due to the excitation of surface plasmon polaritons [36]. At the same time, Kretschmann and Raether reported excitation of surface plasmons in another configuration [36,37]. The pioneer works of Otto, Kretschmann, and Raether on plasmons established a convenient method for the excitation of surface plasmon polaritons. The plasmonics field eventually introduced into modern optics in 1980s when the concept of surface plasmons were first employed for the characterization of thin films [38,39]. The field advances a lot in the following years to the point where surface plasmons have been used to detect single molecules [40]. Surface plasmon resonance (SPR) usually happens where a beam of p-polarized light interact with the interface of a dielectric medium and a metal surface [39]. At the certain angle of incidence, a fraction of the light energy excite the surface electrons in the metal film and make them to oscillate (known as surface plasmon polaritons) [38,39]. After excitation, the oscillation create an electric field in the range of near 300 nm [Penetration depth is plasmon frequency

dependent] between the metal surface and sample (sensing material) and the field propagate parallel to the metal surface [41]. The usual setup of an SPR sensor consist of a prism, metal film, p-polarized light source, optical detector and sample material in contact with the film as demonstrated in Fig. 3.1. The SPR allow us to detect

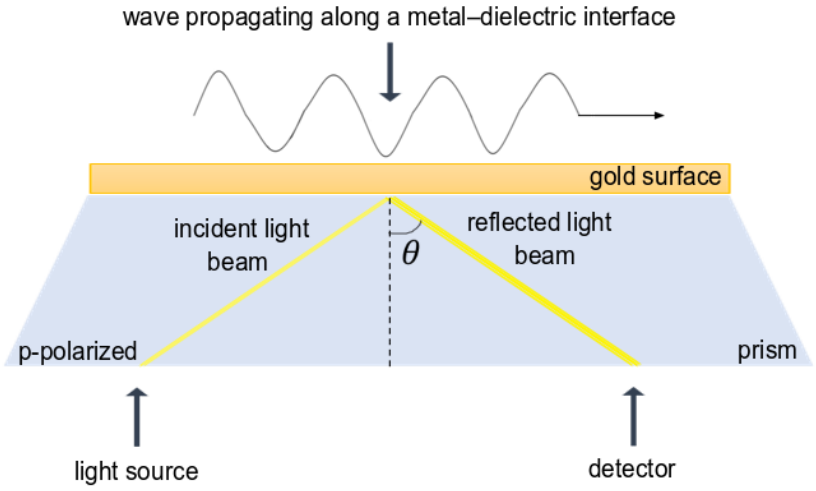

Figure 3.1: Excitation of surface waves close to metal film due to SPR. The setup shows a usual optical setup for SPR sensing including a prism, p-polarized light source, optical detector, and metal film.

materials and objects in real-time with high sensitivity and without the need of labels (label-free detection) [38]. As SPR measures the changes in the RI of a sample close to metal film, it is one of most promising techniques for opaque material detection which can find applications in the fields of biology, chemistry and medicine [39,41]. A surface plasmon polariton wave is a type of electromagnetic waves moving across the surface of a thin metal film [39,41]. At resonance, light energy or reflected intensity is lost as it is imparted to the surface electrons. The resonance (where the oscillation of electrons are maximum) angle or wavelength are extremely sensitive to any change in the RI of the sample which is close to the metal surface. Therefore, the change in RI

of any material can be monitored by recording intensity of the reflected p-polarized light from the interface between metal and dielectric medium [39, 41]. The physical origin of the surface plasmons come from plasma concept in the Maxwell's theory where the free electrons of a metal are treated as an electron liquid of high density (plasma) [39, 41]. In such systems, the density fluctuations on the surface of the materials are called plasmons, surface plasmons (SPs), or surface polaritons [39, 41]. According to the Maxswell's equations, SPs or surface polaritons can propagate near a metallic surface [39, 41]. In order to excite surface plasmon polaritons, the real part of the permittivity of the conductor (metal film) must be negative and its magnitude must be greater than that of the the imaginary part of the permittivity. As noble metals like gold and silver can satisfy these conditions in visible and near IR regions, the condition can be met for air (or water/liquids) and noble metal interfaces if the incoming light beam matches its momentum to that of the plasmon [39, 41]. While s-polarized light cannot excite SPs, the p-polarized light can excite SPs by passing the light through a block of glass to increase its wavenumber (and the momentum), and achieve the resonance at a given wavelength and angle [39, 41].

3.2 Surface plasmon resonance sensors

As SPR is very sensitive to the any change in the RI of the materials attached to the surface of the metal film [38, 42], it can be used as a highly sensitive RI sensing technique for opaque materials. As the conditions of the sensing medium (opaque materials for example) changes, the absorption/intensity maximum location (or spectral response) of the SPR will change accordingly. Therefore, by monitoring the changes in the spectral response of the SPR sensor, we can measure the variations of the sample RI on the surface of a metal film [38, 42]. As such, SPR sensors have made significant contributions to the fields of high-sensitivity spectroscopy, RI

sensing, real-time monitoring and spectral analysis. [42].

3.3 Types of SPR sensors

The SPR sensors are usually designed based on the prism setup. There are two main configurations of the prism-based SPR sensor which are Otto and Kretschmann configurations. Each of these setups has specific design, advantages and disadvantages which will be reviewed in the next subsections.

3.3.1 Otto configuration

In the Otto configuration of SPR, a prism with higher refractive index (n_p) is interfaced with a dielectric–metal waveguide structure consisting of a thin dielectric film with a thickness (q), and a thin metal film with refractive index (n_m), as demonstrated in Fig. 3.2. A light beam incident on the prism-dielectric film interface at

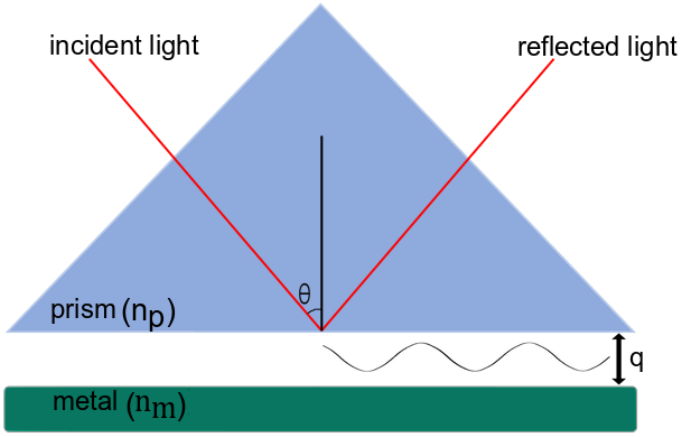

Figure 3.2: A basic setup of Otto configuration for SPR sensors.

an angle of incidence larger than the critical angle of incidence for these two media (total internal reflection) which produces an evanescent wave propagating along the

interface between the prism and the dielectric film [43]. When the thickness of the dielectric layer is right (typically few microns), the evanescent waves and SPs at the dielectric–metal interface can couple and exchange energy. To have coupling, the propagation constant of the evanescent wave and that of the surface plasmon should match (be equal to each other) [43].

3.3.2 Kretschmann configuration

In the Kretschmann configuration, a prism with higher RI is interfaced with a metal dielectric waveguide structure which consist of a thin metal film (usually gold) with refractive index (n_m) and thickness (q) [43, 44]. A basic setup of Kretschmann configuration for SPR sensors is shown in Fig. 3.3.

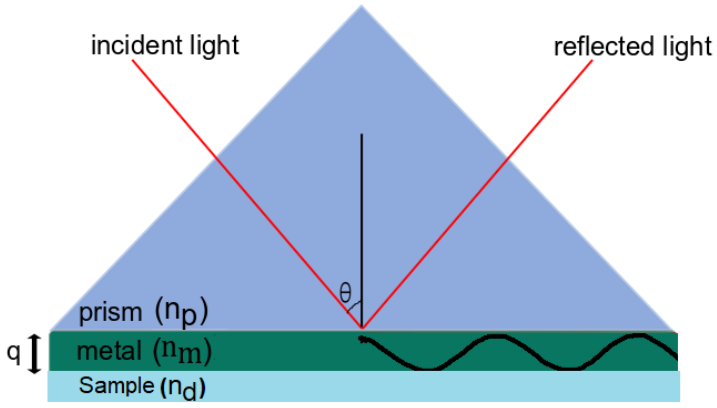

Figure 3.3: A basic setup of Kretschmann configuration for SPR sensors.

When a light beam propagating in the prism hits the metal film, a part of the light beam will be reflected back into the prism and a part propagates in the thin metal film as an evanescent wave which decays exponentially in the direction perpendicular to the prism–metal interface [43, 44]. The evanescent wave penetrates through the metal film and can couple to a surface plasmon polariton (SPP) at the outer side

of the thin metal film [43, 44]. The propagation constant of the SPP (β^{SP}) which is propagating along the thin metal film varies depending on the dielectric material on the opposite side of the metal film and can be expressed as [43, 44]:

$$\beta^{SP} = \beta^{SP_0} + \Delta\beta = \frac{\omega}{c}\sqrt{\frac{\varepsilon_d \varepsilon_m}{\varepsilon_d + \varepsilon_m}} + \Delta\beta \tag{3.1}$$

Where β_{SP_0} is the propagation constant of the SPP which is propagates along the metal–dielectric interface in the absence of the prism, and $\Delta\beta$ accounts for the thickness of the metal film and the presence of the prism [38, 43, 44]. To see the coupling between the evanescent wave and SPP, the propagation constants of the evanescent wave (β_{EW}) and that of the SPP (β_{SP}) have to be equal [43, 44],

$$\frac{2\pi}{\lambda} n_P \sin\theta = k_z = \beta^{EW} = Re\left\{\beta^{SP}\right\} = Re\left\{\frac{2\pi}{\lambda}\sqrt{\frac{\varepsilon_d \varepsilon_m}{\varepsilon_d + \varepsilon_m}} + \Delta\beta\right\} \tag{3.2}$$

If we want to see this coupling condition in terms of refractive indices, we will have [43, 44],

$$\frac{2\pi}{\lambda} n_P \sin\theta = n_{ef}^{EW} = n_{ef}^{SP} = Re\left\{\frac{2\pi}{\lambda}\sqrt{\frac{\varepsilon_d \varepsilon_m}{\varepsilon_d + \varepsilon_m}}\right\} + \Delta n_{ef}^{SP} \tag{3.3}$$

where n_{ef}^{EW} is the effective index of the evanescent wave, n_{ef}^{SP} is the effective index of the SPP, and $\Delta n_{ef}^{SP} = Re\{\Delta\beta\lambda/2\pi\}$. The Kretschmann configuration has a few advantages over Otto configuration. First, as there is no space between metal film and prism, the sensitivity of RI sensing in Kretschmann configuration is usually higher than Otto configuration. In addition, Otto configuration is not suitable for RI sensing in liquids as there is a distance between the prism and the thin metal film in the setup of the sensor. Finally, the Kretschmann configuration is usually easier to setup. Due to these reasons, Kretschmann configuration of SPR is usually the mainstream setup of SPR sensors in different applications which can offer real-time sensing, label-free detection, high sensitivities and easy setup and relatively low cost [43, 44].

3.4 SPR sensors interrogation types

Most of the SPR sensors are based on prism couplers as prism-based coupling of light into SPs is easy and straight-forward where one can use only simple optical elements to realize such sensing systems [43, 44]. There are two main types of interrogation methods in prism-based SPR sensors: angular interrogation method (AIM) and wavelength interrogation method (WIM). In AIM, one should use a monochromatic light source (one single wavelength) as the excitation source. There are three main configurations of AIM SPR sensor. The first type of AIM SPR sensor utilize a monochromatic light source with a fixed angle and study the variations in the intensity in output [37]. The second type of AIM SPR sensor utilize a monochromatic light source and detector which are moving around at the same time to gradually change the angle of incidence of light beams on the metal film at the interface with the prism, as demonstrated in Fig. 3.4 [37]. As the resonance condition of SPs depends on the incident angle, one can expect to see an intensity dip as energy is lost to plasmons at certain incident angle. The peak maximum location will change as we change the RI of our dielectric sample material and therefore, the resonance angle (the angle at which we observe the peak of loss intensity) can be related to the RI of sample. The third type of AIM SPR sensor utilizes a light source like LED and focuses the light beam into the interface (which will create different angles), and then an array of detectors will be used to detect the light at the output [37]. In contrast to AIM, WIM method utilizes a fixed incident angle, a polychromatic light source (with multiple wavelengths) and a collimated beam. In this method, the absorption spectra (and peak wavelength) varies with RI of the sample [43, 44]. Overall, both methods can be used to detect an opaque material using SPR sensors but AIM relates the SPR intensity loss to the incident agnle and WIM relates the SPR intensity loss to the incident wavelength. In the next chapter, we'll talk about a typical WIM mode

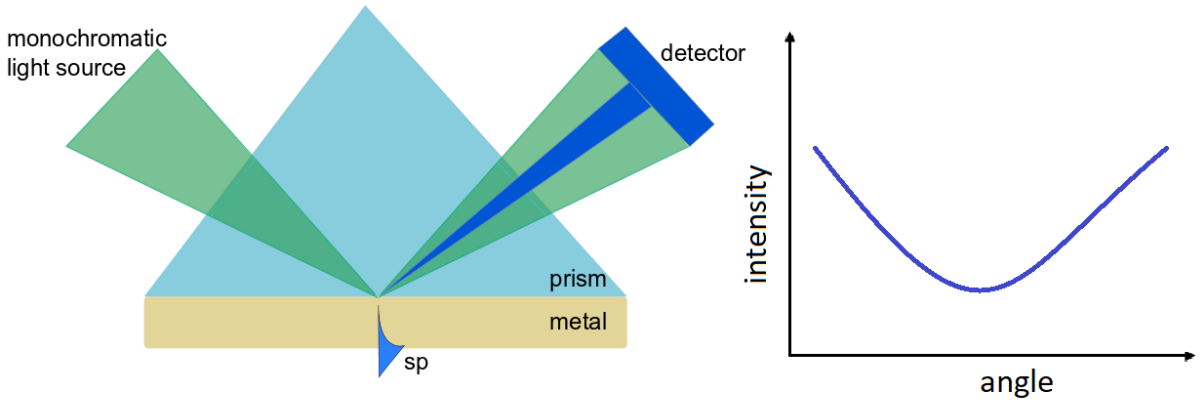

Figure 3.4: Schematic of angular interrogation method in prism-based SPR sensors.

SPR sensor setup and develop a theoretical model to predict the variations in SPR peak wavelength depending on the sample RI.

Chapter 4

Modelling the SPR sensor with the matrix method

The prism-based SPR sensor consist of different media (layers) in the sensing area including prism, metal films and the sample. To find the amplitudes of electric and magnetic fields in each layer, one should solve wave equations propagating in these media. As the number of layers are usually large in SPR sensors, the conventional analysis of wave equations becomes complicated and therefore, there is a need to use alternative methods to find the reflection and transmission of electromagnetic waves, and electric/magnetic field in each medium. Matrix method is a systematic approach to solve such complicated problems using matrix algebra. In this chapter, we first study the Fresnel equations and the concept of reflected/transmitted coefficients, and then discuss modelling of our SPR sensor using the matrix method.

4.1 Fresnel equations

The reflection and transmission of light when incident on an interface between different media can be described using the Fresnel equations [22]. In particular, Fresnel's equations can predict behaviour of electromagnetic waves of the s and p polarizations incident upon an interface between a medium with refractive index n_1 and a second medium with refractive index n_2 [22], as indicated in Figure 4.1. The angles that the incident, reflected and transmitted rays make to the normal of the interface are given as θ_i, θ_r and θ_t, respectively. The equations assume a flat interface between the me-

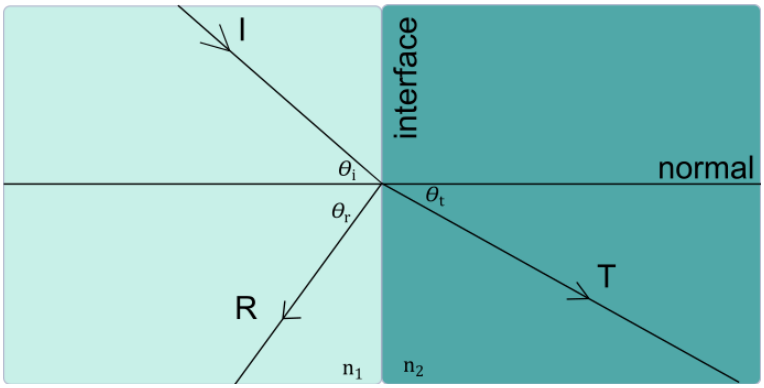

Figure 4.1: Variables used in the Fresnel equations.

dia. The equations also consider that the media are homogeneous and isotropic [22]. Furthermore, the incident light wave is assumed to be a plane wave [22]. Two sets of Fresnel coefficients are exist for two different linear polarization components of the incident light wave [22] as any polarization state can be resolved into a combination of two orthogonal linear polarizations. The s-polarization refers to polarization of an electric field normal to the plane of incidence. The p-polarization refers to the polarization of the electric field in the plane of incidence. The relationship between these angles is given by [22]

$$\theta_r = \theta_i \tag{4.1}$$

and according to Snell's law,

$$n_1 \sin\theta_i = n_2 \sin\theta_t \tag{4.2}$$

The behavior of light (transmission or reflectance) at the interface is solved by considering the electric and magnetic fields [22]. The fraction of the incident power that is reflected from the interface is called the reflectance (or power reflection coefficient) R, and the fraction that is transmitted into the second medium is called the transmittance (or power transmission coefficient) T. If complex refractive indices are used, attenuation is taken into account. [22]. The reflectance for s-polarized light is given

by [22]

$$R_s = \left| \frac{Z_2 \cos\theta_i - Z_1 \cos\theta_t}{Z_2 \cos\theta_i + Z_1 \cos\theta_t} \right|^2 \tag{4.3}$$

The reflectance for p-polarized light is given by [22]

$$R_p = \left| \frac{Z_2 \cos\theta_t - Z_1 \cos\theta_i}{Z_2 \cos\theta_t + Z_1 \cos\theta_i} \right|^2 \tag{4.4}$$

where Z_1 and Z_2 are the wave impedances of media 1 and 2, respectively. Here it is assumed that the media are non-magnetic. Therefore, the wave impedances are determined solely by the refractive indices n_1 and n_2,

$$Z_i = \frac{Z_0}{n_i} \tag{4.5}$$

where Z_0 is the impedance of free space and $i = 1, 2$. The final equations using the refractive indices are given by [22],

$$R_s = \left| \frac{n_1 \cos\theta_i - n_2 \cos\theta_t}{n_1 \cos\theta_i + n_2 \cos\theta_t} \right|^2 = \left| \frac{n_1 \cos\theta_i - n_2 \sqrt{1 - (\frac{n_1}{n_2} \sin\theta)^2}}{n_1 \cos\theta_i + n_2 \sqrt{1 - (\frac{n_1}{n_2} \sin\theta)^2}} \right|^2 \tag{4.6}$$

$$R_p = \left| \frac{n_1 \cos\theta_t - n_2 \cos\theta_i}{n_1 \cos\theta_t + n_2 \cos\theta_i} \right|^2 = \left| \frac{n_1 \sqrt{1 - (\frac{n_1}{n_2} \sin\theta_i)^2} - n_2 \cos\theta_i}{n_1 \sqrt{1 - (\frac{n_1}{n_2} \sin\theta_i)^2} + n_2 \cos\theta_i} \right|^2 \tag{4.7}$$

Finally, as a consequence of conservation of energy, the transmitted power for s-polarized and p-polarized light is simply can be calculated as

$$T_s = 1 - R_s \tag{4.8}$$

and

$$T_p = 1 - R_p \tag{4.9}$$

4.2 SPR sensor model using matrix method

To accurately model our SPR sensor, we used MATLAB implementation of matrix method. The sensor consists of an input light source with a known spectra which will propagate through the layered media in the sensing region of the sensor. Using matrix method, we can predict the output light spectra depending on the sample that we have in the sensing region. The model conceptual diagram of the SPR sensor for detection of phase changes of asphaltene in crude oil is illustrated in Fig. 4.1. We first focus on the sensing area which consist of a sapphire dove prism, gold and titanium thin films, and also the sample/liquids. The reason we used a sapphire dove prism instead of a regular glass prism is to match refractive indices of sample, and thin films, as the refractive index of sapphire is larger than that of the silica. The layered media have two important parameters in the SPR sensor: layer refractive index (n) and layer thickness (d). To accurately model these layered media, we used complex refractive index of sapphire [45], gold [46], and titanium [47] from the literature. These complex refractive indices are also plotted as the function of wavelength in Fig. 4.1. The complex refractive indices of sapphire, gold, titanium and also the sample form the refractive index stack in the model. Each layer has also a thickness (d) which have been taken into account in the model development. For our SPR sensor, the thickness of sapphire substrate, and gold and titanium thin films are 1 mm, ∼50 nm and ∼5 nm, respectively. We used a theoretical formulation using matrix method to model the SPR sensor. The reflected p-polarized light relative intensity from the multilayered media in our sensor can be calculated as [12]:

$$R^p = \frac{I^p_{out}}{I^p_{in}} = |r^p|^2 \tag{4.10}$$

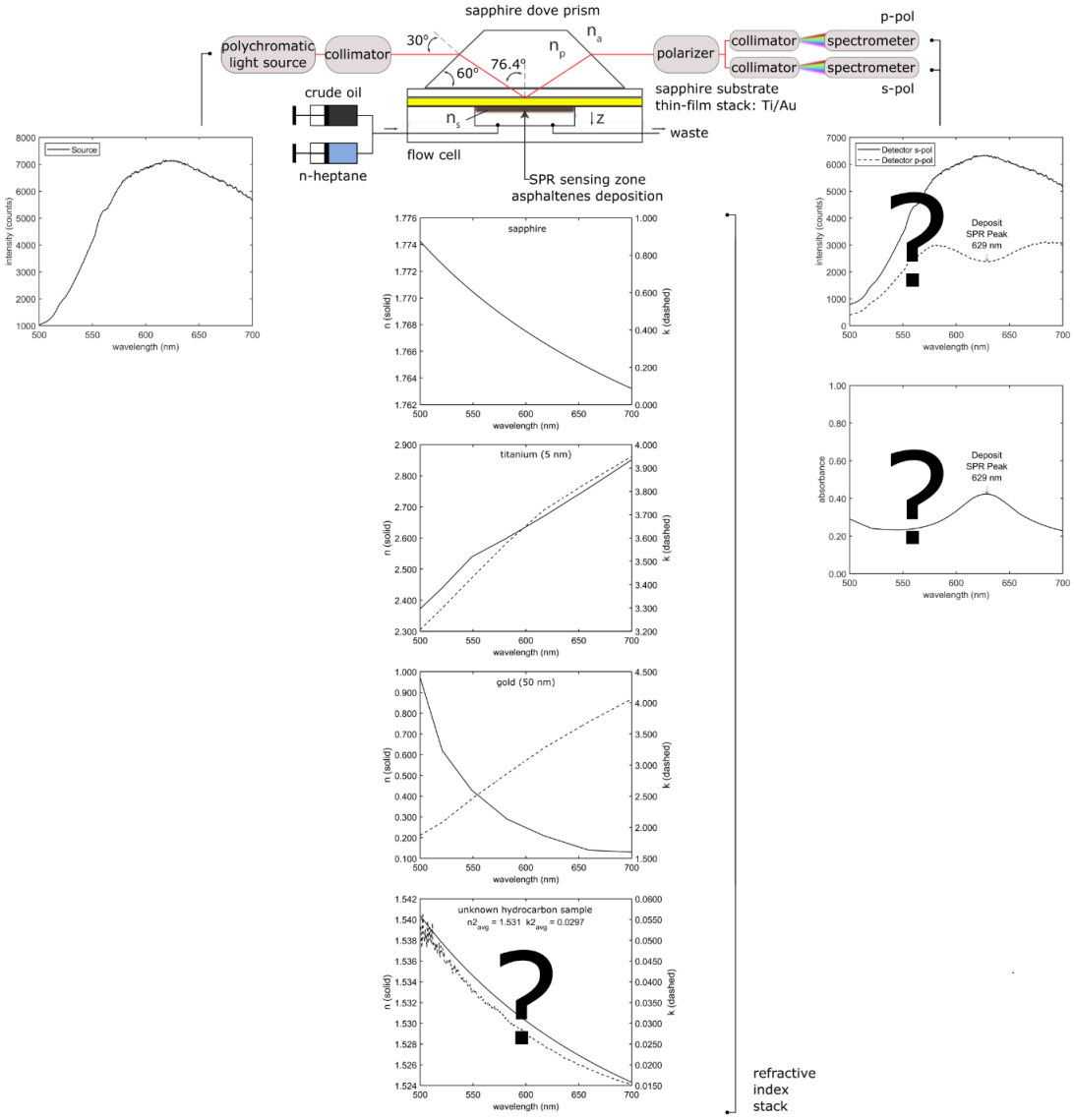

Figure 4.2: Model conceptual diagram, showing input and output light spectra collected based on the matrix formulation and complex refractive indices shown for each layer.

where

$$r^p = \frac{M^p_{21}}{M^p_{11}} \tag{4.11}$$

and

$$\begin{pmatrix} E_i \\ E_r \end{pmatrix} = M^p \begin{pmatrix} E_t \\ 0 \end{pmatrix} \tag{4.12}$$

where R is the relative reflectance at any given angle, I_{in}, and I_{out} are the light intensities of the beam inside the dove prism before and after SPR occurs, respectively. The reflection coefficient is r, and M is the matrix representation of the stack that links the incident, reflected, and transmitted electric field amplitudes (E_i, E_r, E_t). The matrix representation of the stack is calculated as [12]

$$M^p = \begin{pmatrix} M_{11} & M_{12} \\ M_{21} & M_{22} \end{pmatrix} = D_0^{-1} \left[\prod_{l=1}^{N} D_l P_l D_l^{-1} \right] D_s \tag{4.13}$$

$$D_l = \begin{pmatrix} \cos\theta_l & \cos\theta_l \\ n_l & -n_l \end{pmatrix}, \tag{4.14}$$

$$P_l = \begin{pmatrix} e^{ik_l d_l} & 0 \\ 0 & e^{-iK_l d_l} \end{pmatrix}, \tag{4.15}$$

$$k_l = n_l \frac{\omega}{c} \cos\theta_l$$

Where N is the number of layers (l = 0, 1, 2, . . . , s) of the stack. In our SPR setup, the sapphire prism is 0 whereas the final layer (sample layer) is s, which in this case is 3. D_l is the dynamical matrix for each layer l and P_l is the propagation matrix. Dynamical matrix represents the effect of materials on the intensities of reflected and transmitted waves and also polarization effects while the propagation matrix represents absorption and losses in the media. Each layer has n_l, which is the complex index of refraction, θ_l is the complex angle of propagation, k_l is the wave vector along the direction of propagation, d_l is the thickness of the thin metal film, and ω is the angular frequency of the light. Complex refractive indices as functions of wavelengths were used to calculate the refractive indices of the sensor materials. Here, we show one example of how the matrix model can be used to theoretically predict the output absorbance spectra depending on the sample refractive index. We considered a model where the

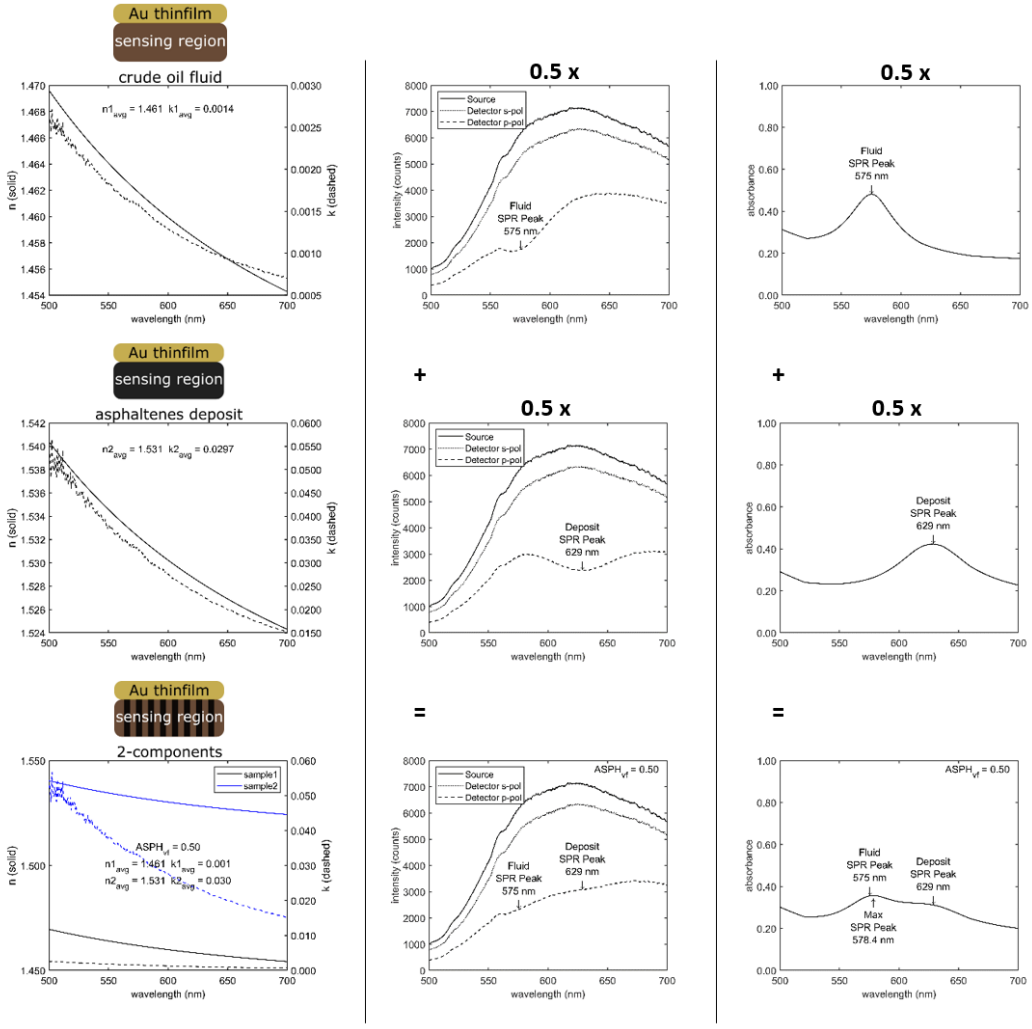

Figure 4.3: Linear superposition model for a two-component system of crude oil fluid and asphaltenes deposit on the SPR sensing surface. The left column shows the model refractive indices (both real and imaginary) used, the middle column shows the resulting intensities calculated from our model, and the right column shows calculated absorbances (-log10[p-pol / s-pol]). Top row represents 100% crude oil. Middle row represents 100% asphaltene deposit. Bottom row represents a 50% crude oil and 50% asphaltene deposit on the SPR sensing surface as shown by the inset figures. The ASPHvf intensity spectrum is equal to 0.5x crude oil intensity spectrum plus 0.5x asphaltene intensity spectrum. The two components are both sensed as the sample is assumed to be comprised of two distinct samples that are not mixed, i.e. in-homogeneous sample in the sensing area.

sensing region consist of a gold thin film and a sample (crude oil with asphaltene in this case), as shown in Fig. 4.2. The samples were modelled with complex refractive

indices are shown in the left column while the calculated intensities are in the middle column and the resulted absorbances are in the right column. When our sample is 100% crude oil (top row) or 100% asphaltene (middle row), the calcluated absorbance spectra has only one peak which is around 575 nm for neat fluidic crude oil, and 629 nm for the deposited asphaltene. However, when the two components are present in the sensing region, the calculated absorbance spectra will show two distinct peaks around 575 and 629 nm. These theoretical predication are in agreement with our experimental observations which will be presented in Chapters 5 and 6. As 1 nm was the resolution on our spectrometer and according to theoretical model when all layers present, we can expect to observe a 0.0022 shift in the refractive index with a 1 nm change in SPR peak wavelength. This means 2.2 mRIU is the limit of detectable shifts in RI of opaque materials in our sensor.

Chapter 5

SPR sensor design, characterization and data analysis

In SPR sensors, data analysis are important as absorption spectra and SPR peak wavelengths are not a direct output of the sensor. The raw output data of the spectrometer is intensities and therefore, we need to obtain the absorption spectra using data analysis. As mentioned in the previous chapter, our SPR sensor is consist of an input light source (white reference) which will propagate through the layered media in the sensing region of the sensor, and depending on the sample characteristics will result in a unique output intensity spectra. Fig. 5.1 represents the schematic of the SPR sensor with input and output light spectra. In the experiments, we used

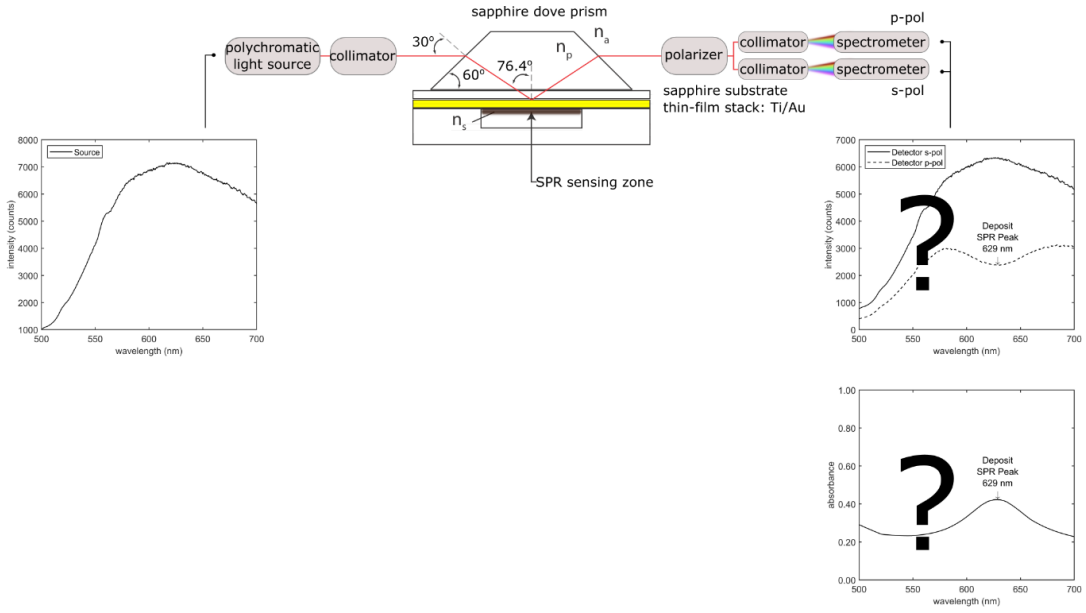

Figure 5.1: Schematic of the SPR sensor setup showing input and output light spectra collected depending on the sample characteristics.

the WIM interrogation method. This setup was selected over an AIM as it avoids the use of moving parts, provides faster acquisition times, and is more robust than AIM SPR sensors. The photograph of the actual SPR sensor setup for evaluating the crude oil asphaltene deposition is depicted in Fig. 5.2. This setup consist of

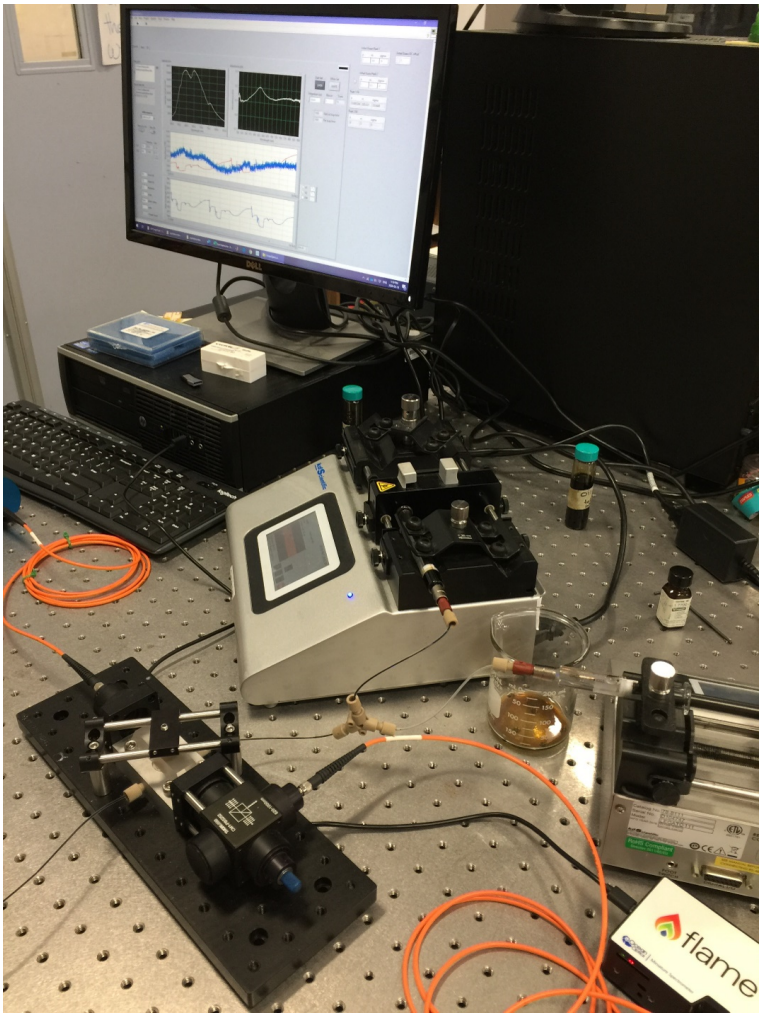

Figure 5.2: Photograph of test apparatus with SPR sensor element at the top of the flow line. The SPR sensing surface is at the top of the sensing line to measure deposition, while minimizing impact from gravitational settling and accumulation.

a flow line (for injection of liquid samples), sensing zone (including sensing layers, Au, Ti, and sapphire), a light source, fiber optic cables to guide the light into the prism and guide the reflected light to the spectrometer, an optical spectrometer and

also the PC to analyse the data using the custom program. A polychromatic light source (HL-2000 tungsten halogen white-light source 360–2400 nm, Ocean Optics, USA) was used in conjunction with an UV–Vis spectrometer (FLAME-S-UV–VIS, Ocean Optics usable range 200–850 nm) to acquire the p-polarized light. Light from the polychromatic light source is fed to a collimator (F240SMA-B, Thorlabs, USA) using a 2 m long 0.22NA-200 µm core SMA-SMA fiber optical patch cable (M92L02, Thorlabs, USA) and is then passed through an adjustable iris (SM1D12D, Thorlabs, USA) which results in a 3 mm diameter beam. The resulting light beam is coupled to a custom made sapphire prism (Meller Optics Inc., USA) which has a side of 70.81 mm, a width and height of 15 mm. a short side of 53.49 mm and angled faces at 60° to the long side. The crystallographic orientation is that the c-plane is aligned to the 70.81 × 15 mm and 53.49 × 15 mm faces. The incident beam is then coupled to a 1 mm thick, 19 mm diameter sapphire substrate with a metallic layer. Index matching fluid (18152, Cargille, USA) with a refractive index of 1.77 (nD20) is used between the prism and the thin metal film. The plasmon resonance occurs in a metallic thin-film stack $\sim 55nm$ thick, which is made up of $\sim 5nm$ of titanium (adhesion layer) and a $\sim 50nm$ of gold layer (primary plasmonic layer) (Deposition Research Lab Inc., USA) which is what comes into contact with the analyte. As light reflects off the metallic thin-film, it is sent through a polarizer (CM1-PBS252, Thorlabs, USA) and the p-polarized light output is detected by the UV–Vis Flame spectrometer. We calculated the absorbance at all the wavelength values by obtaining the white and dark references using a single spectrometer. In spectrometers, a dark measurement captures the intensity when the light source is off or blocked, and a typical intensity for a dark measurement in our sensor is around 2900 pixel counts. In contrast to a dark measurement, a light measurement captures the intensity when the light source is on. A typical intensity for a light measurement in our sensor is around 50,000

pixel counts. In the experiments, the SPR sensor was flushed with toluene and then cleared with compressed air prior to obtaining the white and dark references to ensure no substances were on the sensor surface when the references were taken. Labview first recorded the intensities, once per second where the integration time is set to 60000 μs and data was recorded as the average of 15 samples. The range of intensity values in experiments are between 2500 and 60,000 pixel counts. The UV-Vis Flame spectrometer can detect the p-polarized output light intensities in the experiments. To record and analyse the data, a custom LabView program (2019 version) was developed. To find the SPR peak, LabView calculated the absorbance from the raw intensity which had been recorded and then using formula below absorbance of the experiment had been calculated

$$A_\lambda = -log_{10}(\frac{S_\lambda - D_\lambda}{W_\lambda - D_\lambda}) \tag{5.1}$$

where A_λ is absorbance at wavelength λ, S_λ is the signal intensity, D_λ is the dark reference intensity, and W_λ is the white reference intensity. The LabVIEW program

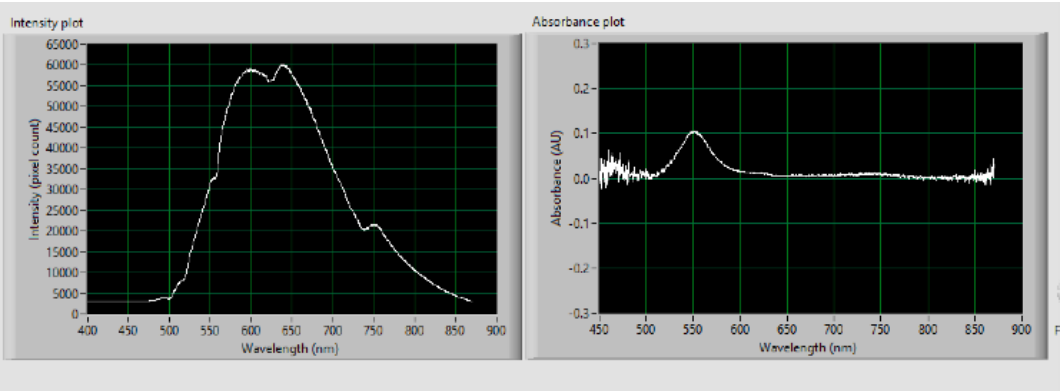

Figure 5.3: Intensity and absorption spectra detected via the LabVIEW program.

was used to record and analyze the spectra measured by the spectrometer. As seen in Fig. 5.3, the program record intensity and calculate the absorbance to track the SPR peak wavelength. In the LabView program, we started with the ocean optics VIs which allow us to work with spectrometer through the LabVIEW as seen in Fig.

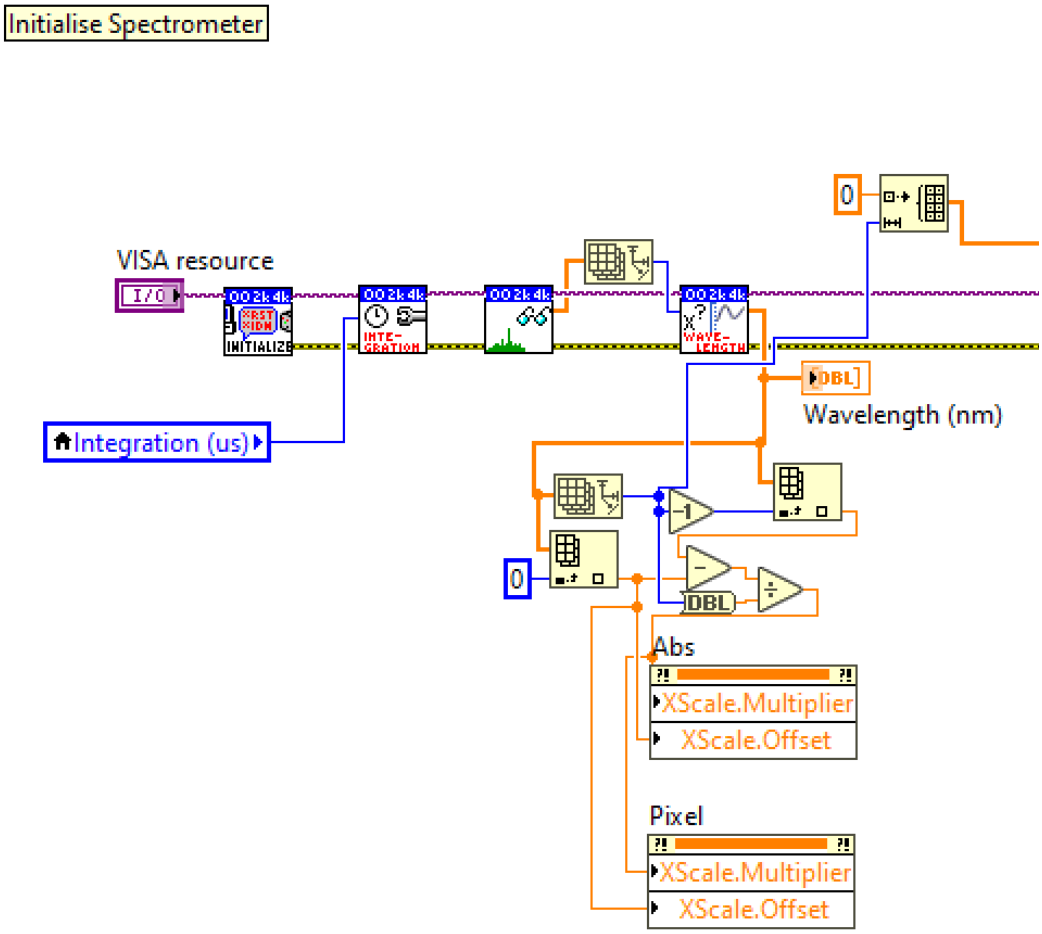

Figure 5.4: Oean Optics VI in the LabView program for using spectrometer and detecting intensity of the light and absorption spectra.

5.4. The SPR peak was determined using LabView's Peak Detector VI algorithm on the absorption spectra, which is demonstrated in Fig. 5.5. The threshold for the absorbance peak was 0.05 while the minimum width was set to 200($\sim 100nm$). By using peak detection function at the range of 500 nm-700 nm, LabVIEW could detect the absorption peak which is also the SPR peak wavelength. Plotting the SPR peak against time allows for an analysis of the ratio for the first time the opaque material attached itself to the gold. For a dual peak detection, we used a nonlinear curve fit VI in LabView. The VI uses the Levenberg-Marquardt method to determine the set of

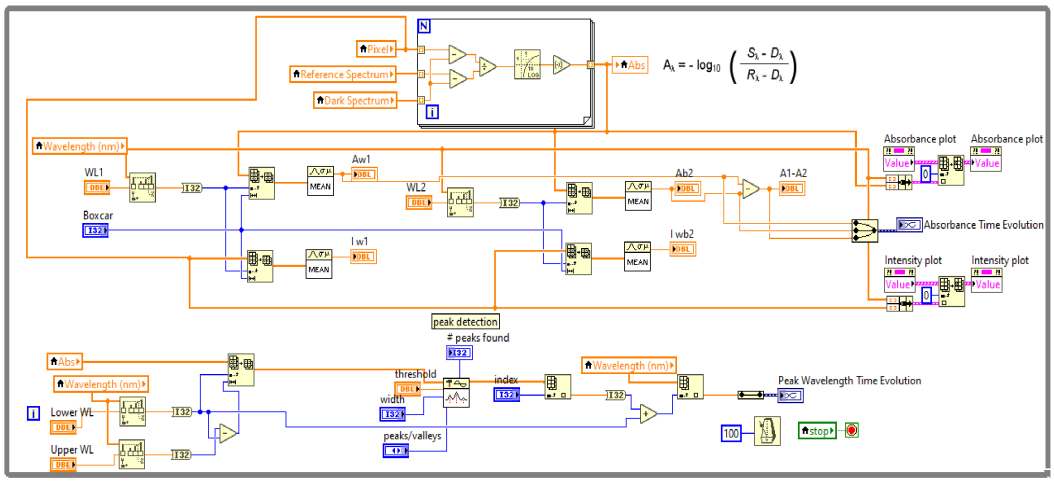

Figure 5.5: The LabView program for detecting the absorption peak.

parameters that best fit the input data set as expressed by a nonlinear function. The customized LabView program can then detect two absorption peaks from one data set (for example crude oil and asphaltene absorption peaks). Using this method, absorption peak locations are well approximated as the residuals from fitting is on the order of 10^{-5}.

5.1 Sensor calibration

5.1.1 n-heptane-toluene measurements

In order to calibrate the sensor, a step wise flow regime at different volumetric ratios of n-heptane-toluene was performed. Here we measured the SPR peak variations of a mixture of heptane (n-C7) and toluene at different volume fractions. It should be noted that absorbance peak is the maximum plasmon polariton resonance, i.e. the most loss of light intensity. We repeat this experiment three times to obtain a range of variation for the data. The SPR peak wavelength is almost 551 nm where the volume fraction is equal to 0 (neat n-C7). As we gradually increase the volume fraction of

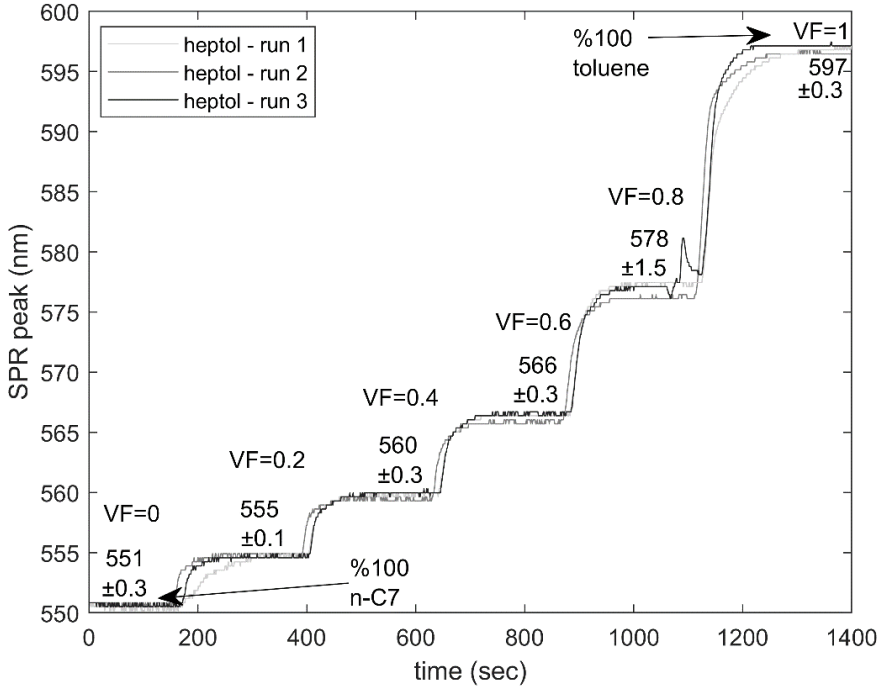

Figure 5.6: Triplicate run of heptane (n-C7) and toluene at different volume fractions.

tolune, this SPR peak shifts towards longer wavelengths. When the volume fraction is equal to 1 (neat toluene), the SPR peak wavelength is almost 597 nm. The raw data from Figure 5.6 leads to obtaining SPR wavelengths for heptane toluene mixture at different ratios. The calibration is then used to tune the theoretical model of the SPR sensor, where we calibrate the SPR peak wavelength against the RI of the same known liquid mixture (heptane and toluene). We used an accurate theoretical model for the experiment and demonstrate the agreement with the results using heptane and toluene, shown in Fig. 5.7.

5.1.2 Crude oil measurements

Heptane and toluene are not opaque and do not have an imaginary RI component. However, this is not entirely correct for our opaque materials such as crude oil. Crude oils (and ashphaltene) typically have a black or brown color and absorb strongly

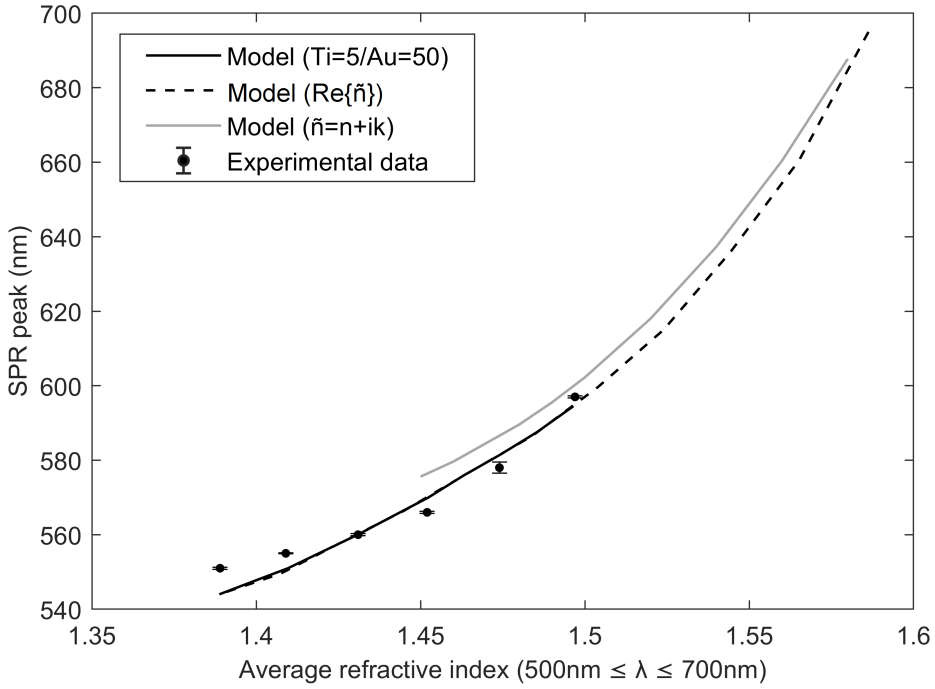

Figure 5.7: Experimental SPR peak wavelength values (solid dots) for different ratios of n-heptane and toluene mixture and comparison to the model calculations (black solid line). Also shown are the SPR calculations for our model asphaltenes, both using a real component only model of the refractive index (dashed line) and using a complete complex refractive index (gray solid line). Error bars represent the standard deviation from a triplicate measurement; data shown in Fig. 5.8.

from 500 nm to 700 nm. Previously, the mass attenuation coefficient of asphaltenes estimated to be approximately $3.0 L.g^{-1}.cm^{-1}$ at 590 nm [48, 49] near our SPR peak wavelengths, with the light absorbance spectra decaying exponentially from the visible toward the infrared. From this, we calculate the asphaltenes imaginary part of the refractive index from the absorbance data in reference [49] and determine it decreases exponentially from $n_I = 0.053$ at 500 nm to $n_I = 0.015$ at 700 nm. Our model then tunes the real part of the complex refractive index to match the SPR peak; for example, $n_{avg} = 1.531 + 0.030\text{i}$ (500 to 700 nm) to yield an SPR peak at 629 nm. The model calculation of the SPR peak wavelength from the average complex refractive index is shown in Fig. 5.7. The real part of the refractive index is determined using

a multiplier applied to toluene's refractive index, which emulates the decaying shape expected. The addition of the absorption parameter via the complex refractive index results in $\sim$ 6-7 nm shifts of the SPR peak wavelength, from 622 nm using only a real refractive index to 629 nm using a complete complex refractive index. The complex refractive index also introduces broadening of the SPR peaks, aligning our model calculations more closely to our experimental observations. The neat crude oil's imaginary part remains insignificant and does not shift the SPR peak for low asphaltene content crude oils. For the crude oil used in this study, we calculated it to be $n_{I_{avg}} = 0.001$, and the crude oil fluid SPR peak remains at 575 nm when using either real only refractive indices or complex refractive indices. For the figures in the thesis, the real only refractive index was plotted on the second y-axis to link with the observed SPR peak on the first y-axis.

5.2 Noise from the SPR experiments

During the measurements using SPR sensor, we repeated the experiments to evaluate the repeatibility and reliability of the sensor. All experimental data presented here were collected from three different sapphire/Ti/Au substrates, each producing nearly identical SPR peaks for the toluene and n-heptane calibrations. The standard deviation of SPR (absorption) peak measurements for three repeated runs is ($\pm$0.6 nm) which means the error is rather small in the experiments. The results of these triple runs are demonstrated in Fig. 5.8. The small variations of SPR peak in the experiments ($\pm$0.6 nm) is possibly comes from the signal noise in the experiments. The noise can potentially comes from small variations in the syringe pump speed, or inherent noise of the light source.

Between different crude oil titration runs, the surface was readily cleaned with toluene and reused for multiple experiments. Typically, 20 to 30 runs are possible before

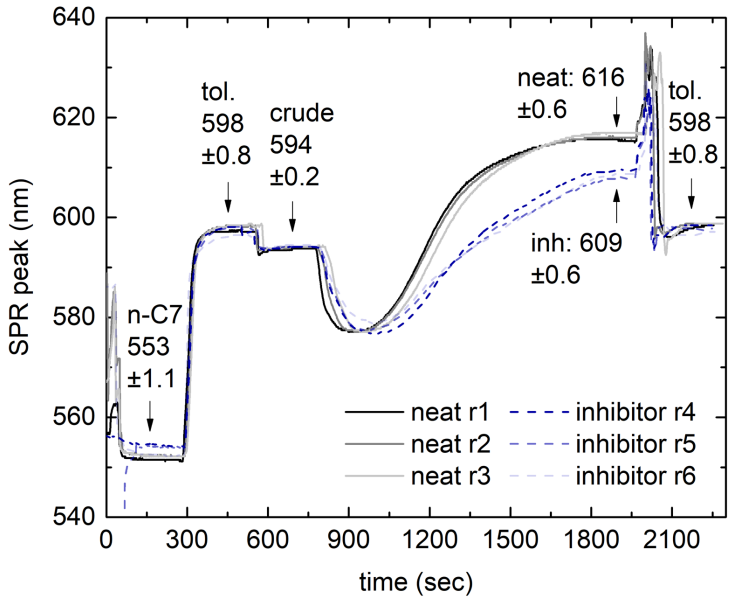

Figure 5.8: Three consecutive runs of ramped n-heptane titrations of neat crude (r1 to r3) and three consecutive runs of ramped n-heptane titrations of crude oil dosed with 10,000 ppm of Inhibitor 5 (r4 to r6). The stages of fluid delivery were according to Table 6.1. First, n-C7 is flowed through the flow cell for 4-minutes, followed by toluene and crude oil, each for another 4-minutes, respectively. Next, the ramped titration is completed over 20 minutes, observed by the dip and graduate rise in SPR peak wavelength as the deposition is formed. Finally, the system is flushed and cleaned with toluene. A high concentration of inhibitor was chosen to determine if the asphaltene onset point could be shifted compared to the 1,000 ppm used in the manuscript. It would appear that at high dosages a slight delay of the onset is notable. The average SPR peak wavelength and standard deviation shown at each arrow is for all 6 measurements (where common fluids were sensed), except for the plateaus that represent 3 measurements (different deposits). Each measurement was acquired by averaging the last 30 seconds of each run at each stage. Data was acquired from a different aliquot/batch of the stock tank crude oil sample used in the manuscript; however, it highlights the repeatability of the measurement.

noticing physical damaged due to repeated handling. The detailed explanation of the theoretical model can be found in Chapter 4 of this thesis. For the n-heptane and toluene calibration runs, the absorption from 500 nm - 700 nm is negligible and the imaginary part of their refractive indices are neglected. According to the model and as seen in Fig. 5.7, by increasing the average refractive index of the sample (n_{avg} from

500 nm $\leq \lambda \leq$ 700 nm), the SPR peak wavelength shifts towards longer wavelengths. Therefore, by measuring the SPR peak wavelength of an unknown substrate, we can calculate and determine the refractive index of the sample using our model. In Fig. 5.7, the model shows SPR peak wavelength values for a range of average refractive indices between n-heptane ($n_{avg} = 1.389$) and toluene ($n_{avg} = 1.497$). To extend our model to a higher range of refractive indices, we used 1.06 times that of toluene ($n_{avg} = 1.587$), shown by the dotted line in Fig. 5.7. In both model and extended model calculations, the Lorenz-Lorentz volumetric mixing rules were used to generate the refractive indices versus wavelength of the final sample sensed. In the next section, the application of our SPR sensor in oil industry will be investigated in detail.

Chapter 6

Application of SPR sensor in oil industry: study the role of inhibitors on asphaltene deposition from crude oil

This chapter resulted in the following publication: Fuel, Volume 273, 1 August 2020, 117787

https://doi.org/10.1016/j.fuel.2020.117787

In this chapter, we present a direct method for evaluating the effectiveness of inhibitors on asphaltene deposition from crude oil based on a Kretschmann configuration surface plasmon resonance (SPR) sensor. We demonstrate that shifts in the peak SPR wavelength during titration experiments can be used to compare inhibitors, both by changes to the deposition temporal profile and by changes to the refractive index of the final deposit. We continually measure the SPR peak wavelength throughout the entire titration experiment, starting with that of the neat crude oil and gradually ramping through a pre-defined range of n-heptane to crude oil fractions. After the deposition onset point, asphaltenes precipitate and are deposited onto the sensing surface, which results in an SPR peak wavelength increase as the refractive index of the deposit on the sensing surface increases. The asphaltenes continue to deposit on the surface until the deposit completely fills the SPR field penetration depth. We

observe a change in the asphaltene deposition profile and also the final average refractive index of the deposit when inhibitors are added to the neat crude oil and the same titration experiment is conducted. We also qualitatively describe the asphaltene deposition mechanism using SPR spectral data. SPR provides a new and powerful sensing approach for screening and comparing the effectiveness of asphaltene deposition inhibitors.

6.1 Background and motivation

Formation of organic deposits during petroleum production can cause several operational troubles, such as total or partial blocking of pipelines and equipment damage, which usually leads to substantial financial costs [50]. The heaviest molecular weight fraction of crude oil is asphaltenes that have aggregative characteristics and form surface depositions in wells, pipelines, and facilities [50, 51]. Changes in pressure, temperature and composition cause a shift in the asphaltene solubility in the crude oil, which results in asphaltenes precipitation [52]. Precipitation can then lead to asphaltene deposition that causes fouling in the flowlines and may even lead to plugging and failure of equipment [52]. There are a variety of deposition remediation methods, including: mechanical cleaning [53], cleaning with solvents [54], removal with hot fluids or water steam [55, 56]. Generally, it is preferable to prevent the onset of asphaltene deposition using inhibitors [57–59]. The main function of inhibitors is to alter the aggregation kinetics [57–59]. The functionality of inhibitors depends mainly on their structural and chemical characteristics. Current screening approaches select ideal chemicals based on their ability to prevent or slow down flocculation and sedimentation, eg. Turbiscan and ASTMD7061-06. However, these laboratory tests do not measure deposition tendency and often do not relate well to the field observations. Even though a variety of inhibitors have been investigated in the literature [59–61],

measuring the effectiveness of inhibitors as relates to the onset of asphaltene deposition and to the density of deposited layer would provide insight in screening and evaluating inhibitors. The asphaltene subfractions are difficult to classify and are therefore defined/bounded by their solubility profile. Typically, they are characterized as being soluble in toluene, while precipitating in excess amounts of n-alkanes (e.g. n-heptane). N-heptane titration or depressurization of oil is usually needed to determine the solubility of the asphaltenes in certain oils [52]. The more n-heptane needed, the more soluble the asphaltenes are and therefore the more stable they are. The degree of asphaltene precipitation can be detected and measured using different methods such as fluorescence spectroscopy [62, 63], light scattering [64], refractive index-based methods [65], acoustic resonance [66] and the conventional gravimetric technique [67]. However, in order to monitor and study asphaltene deposition on a surface in real-time, these conventional methods cannot be directly utilized. Instead methods like quartz crystal microbalance with dissipation (QCM-D), Taylor-Couette devices/chambers and long-tube/capillary experimental setups are used to study deposition. It is also important to note that stock tank crude oil analysis/studies are limited in scope and do not account for solution gas from either natural or artificial gas injections. In a previous manuscript we address the advantages of using surface plasmon resonance (SPR) compared to the above methodologies and the ability of SPR sensing to be applied at live oil conditions [12]. Using SPR [12, 68, 69], one can detect the onset of asphaltene deposition along with the refractive index of the deposit. This technique allows for accurate real-time measurements of the asphaltene deposition without the need of complex setups [68, 69]. The SPR sensor is sensitive to slight changes in the refractive index near the surface of a thin-metal layer, and as such, it can be used to monitor asphaltenes as they begin to be deposited [12]. Due to the evanescent wave created during SPR, the sensor is sensitive only to media near the chip surface. For example, the plasmon resonance described in the present study

occurs in the visible spectrum between 500 and 700 nm; however, the penetration depth of the field is confined to 100 to 300 nm into the media. If the sample fluid was toluene in our previous setup, the penetration depth would be d_p =115 nm for λ=590 nm and d_p=289 nm for λ=800 nm [12]. Therefore, the SPR technique can detect asphaltene deposits of a few nanometers to a few hundred nanometers thick. This means SPR sensors can be used to detect the early stage aggregation and deposition events as they begin. As more and more asphaltenes precipitate, aggregate and attach themselves to the sensor, a further change in the SPR peak absorbance wavelength is measured. The denser the deposit sample, the higher the SPR peak wavelength. There is a limit, observed as a plateau in the SPR peak wavelength (i.e. a constant value with respect to time), which indicates that the asphaltenes deposit has filled up the sensing region or depth of the sensor penetration field. This information can be used to determine the asphaltene deposition rate of the samples, as well as the refractive index of the deposit. In this chapter, we show a novel screening approach that is utilized to evaluate different asphaltene inhibitors. Further, the SPR sensor is used to study the effects inhibitors have on the overall crude oil asphaltene deposition profile and final deposit refractive index. To accurately study the asphaltene deposition mechanism, we used both a ramping-titration and constant n-heptane titration to induce the asphaltenes to precipitate and attach to the sensor surface. We have investigated different titration regimes: before deposition onset, near onset and clearly after deposition onset. Our results indicate that SPR sensors can screen the inhibitors for finding candidates that significantly reduce the asphaltene deposition rate and lower the overall refractive index/density of the final deposit from a crude oil.

6.2 Methodology

6.2.1 Samples

Five proprietary and commercially available inhibitor samples were used in this study to examine their effects on slowing asphaltenes deposition from crude oil. The inhibitors are labeled 1 through 5 in this thesis. The crude oil sample used in this study was provided by Schlumberger (Boston, MA). The sample had a saturates content of 49.9 wt%, an aromatics content of 38.3 wt%, a resins content of 9.6 wt% and an asphaltenes content of 2.2 wt%. For all experiments in this manuscript, the inhibitors were added to the crude oil to achieve a final concentration of 1000 ppm. Work by Madhi et al. showed that certain inhibitors like Cetyl Trimethyl Ammonium Bromide (CTAB) and Sodium Dodecyl Sulfate (SDS) had optimal concentrations around 600 ppm of CTAB and 300 ppm of SDS for the crude oils used in their study [58]. The 1000 ppm used here is therefore a reasonable concentration for initially studying the deposition of asphaltenes, although it would be more economical to use a fraction of this (100–200 ppm) in field conditions. Similarly, Yen et al. showed a field study using 250 ppm and laboratory experiments at 2000 ppm to evaluate inhibitor effectiveness [70]. Our inhibitors were first diluted in toluene to achieve a 10% (v/v) mixture. The various inhibitor mixtures were then introduced to the crude oil; 0.6 mL of inhibitor/toluene mixture was added to 5.4 mL of stock tank crude oil. Diluting the inhibitor in toluene facilitated mixing of the inhibitor with the crude oil. The control, referred to as neat crude hereafter, in this study was 90% (v/v) stock tank crude oil and 10% (v/v) toluene. The solvents used were HPLC grade toluene (CAS # 108-88-3) and HPLC grade n-heptane (CAS # 142-82-5) acquired through Fisher Scientific.

6.2.2 SPR sensor setup

We utilize a wavelength interrogation mode (WIM) SPR sensor optimized for crude oil samples described in the previous chapter, where a thin gold film is backlit for sensing the index of refraction of a fluid on the other side of the gold [12]. The WIM-SPR used in testing was designed to detect refractive indices in the range of 1.4 to 1.7. The SPR sensor setup is explained in Chapter 5 in detail. Here we describe the specifics of the setup of injecting the samples in crude oil application. Two syringe pumps (Legato 270 and 111, KD-Scientific, USA) with either 10 mL, 5 mL, or 1 mL syringes (Hamilton 1001, 1005, and 1010, USA) were used to induce fluid flow into the sensor. A single pump was used solely for pumping n-heptane while the other pump delivered either crude oil or toluene, pre-loaded in separate syringes. The n-heptane syringe and the sample syringe were connected to a Y-connector with 150 mm of 0.762 mm I.D FEP tubing from each pump, and the output line connected to the SPR sensor with 150 mm of 0.762 mm I.D FEP tubing. The flow cell used in the SPR sensor is an aluminum block (Protolabs, USA) which had a total internal dead-volume of 42.5 µL. The flow cell had an opening on top of the fluid flow with an internal diameter of 4 mm and depth of 0.5 mm so that the fluid could come into contact with the thin-metal film in the SPR setup. The opening was placed on top of the flow to help eliminate and minimize gravitational settling as a means for detecting deposition. The waste of the SPR sensor was sent to a waste bottle with the same FEP tubing. The experimental setup described is shown in Fig. 6.1.

6.2.3 Procedure

Data analysis has been discussed in Chapter 5 of this thesis. Here, we briefly describe the experimental procedure for this study. In this study, we used a single spectrometer

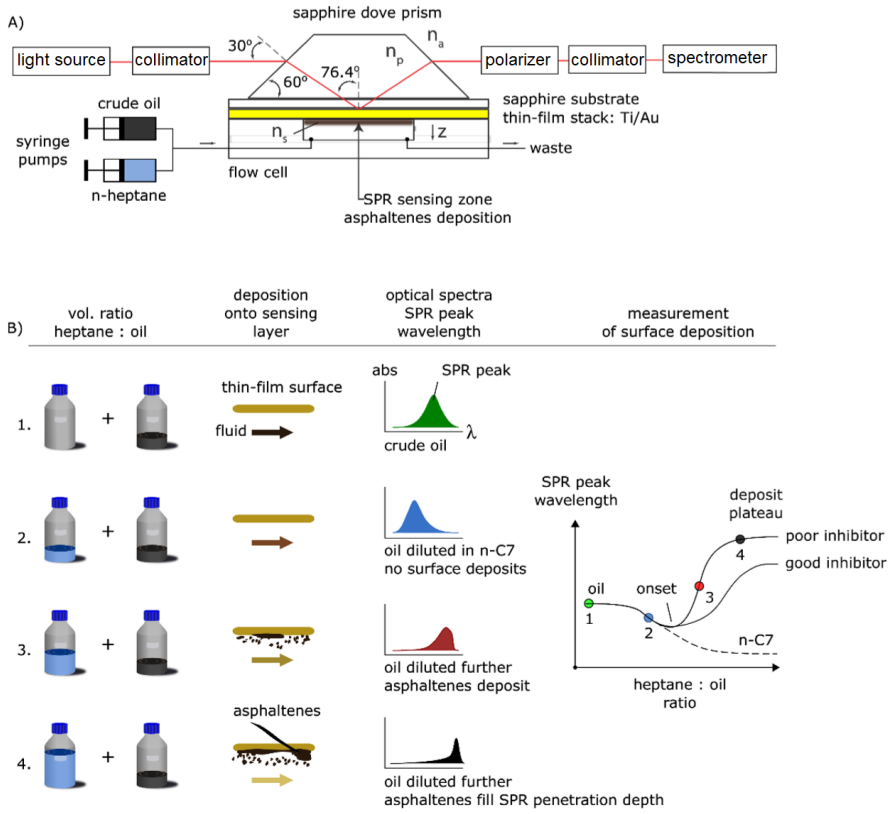

Figure 6.1: (A) Schematic diagram of the experimental setup and (B) concept of SPR sensor for measuring asphaltenes deposition onset, and the effects of inhibitor on asphaltene deposition rate and depth.

and acquire white and dark references to calculate the absorbance at each wavelength. The SPR sensor was flushed with toluene and then cleared with compressed air prior to obtaining the white and dark references to ensure no substances were on the sensor surface when the references were taken. At the beginning of each run, a n-heptane flush would be performed at 250 $\mu L/min$ for 4 min to bring titrant to the Y-connector junction, preventing any backflow from the toluene/crude oil line. A similar prime flush at the same flowrate and duration was also performed with toluene, followed by crude oil. Therefore, at the start of each titration, the lines were primed and neat crude oil was loaded in the SPR sensor. The details of the procedure are summarized

Crude Oil Asphaltene Deposition		
Steps	Description	Length
1	Flush sensor with hep @ 0.250 ml/min	4 min
2	Flush sensor with tol @ 0.250 ml/min	4 min
3	Flush sensor with oil sample @ 0.250 ml/min	4 min
4*	Pump oil sample starting from 0.230 ml/min to 0.130 ml/min	20min*
4*	Pump heptane starting from 0.020 ml/min to 0.120 ml/min	20min*
5	Flush sensor with tol @ 0.250 ml/min	4 min

Table 6.1: Procedure of mixing samples and running experiments.(*occurring simultaneously).

in Table 6.1. The titration portion of the process was then started, which consisted of staring the n-heptane at 20 $\mu L/min$ and linearly ramping up to 130 $\mu L/min$ over the course of 20 min. Conversely, the crude oil flow rate began at 230 $\mu L/min$ and linearly ramped down to 120 $\mu L/min$ over the 20 min to keep a constant 250 $\mu L/min$ flowing through the flow cell at all times. This yielded a heptane-oil volume ratio sweep of 0.09 to 1.08. Please note that this equates to a n-heptane volume fraction range of $V_{f-nC7} = 0.08$ to 0.52. The mixing time of the crude oil sample and n-heptane was 26.6 s, from Y-junction to sensor output, and the whole run (with priming) lasted 36 min. Since the combined flow of the liquids is in the laminar region, mixing is largely dependent on diffusion across the cross-sectional area of the tube. Using n-heptane as the defining solvent in determining the characteristic time for mixing, the root-mean-square distance traversed, or the characteristic 2-dimensional diffusion length, for the n-heptane molecules is 0.36 mm. This value was obtained using the n-heptane self-diffusion coefficient at 20–25 °C of 3.1 X 10^5 cm^2/sec [51] and a transit time of 26.6 s from Y-junction output to SPR sensor inlet. Therefore, sufficient mixing of the fluids occurred. Fig. 6.1B shows the simplified mechanism behind the SPR sensor titration measurements. At the beginning of the titration, the flow is mostly crude oil. This is seen in Fig. 6.1B-1 as the SPR peak will occur at a higher wavelength than n-heptane, as the crude oil is typically denser. As the oil

begins to become more and more diluted with the n-heptane, the SPR peak begins to shift to lower wavelengths (Fig. 6.1B-2) since the refractive index (density) of the overall solution decreases. However, at a certain point in the titration, the SPR peak wavelength stops decreasing and instead begins to rise even though it is being continuously diluted as seen in Fig. 6.1B-3. This is due to the n-heptane precipitating the heavier asphaltene-subfraction of crude oil, which subsequently deposits on the SPR sensor thin-film metal. Since the asphaltenes have a higher refractive index than the n-heptane-oil mixture, the wavelength with the SPR peak rises as more and more asphaltenes attach themselves to the sensor. At a certain point, however, the SPR peak wavelength remains constant even though the heptane-oil ratio continues to change (Fig. 6.1B-4). This is due to the deposited asphaltenes occupying the extent of the SPR field penetration depth. Therefore, further deposition cannot be observed as the sensor cannot detect change in refractive indices beyond the sensing field. The SPR peak was determined using LabVIEW's Peak Detector VI algorithm on the absorbance curve, according to the data analysis procedure explained in Chapter 5. Plotting this SPR peak against time allows for an analysis of the ratio where deposition onset occurs and can be used to calculate the refractive index of sensed analyte and any given time. We performed our experiments with SPR sensor in room temperature. While the complex refractive index of gold, sapphire, and Ti change with temperature, the Kretschmann configuration of SPR sensor (the instrument) is almost insensitive to small temperature variations [71]. A similar stack (50 nm metal and prism) showed approximately 7 nm SPR peak shift with a 100 degree of Celsius temperature variations from 26 degree to 126 degree of Celsius [71]. However, changes in the temperature can modify the refractive index of the sample, especially if the sample is in liquid state like crude oil. It has been demonstrated that the RI of light crude oil can change from 1.4530 to 1.4492 by a temperature increase from 20 to 30 degree of Celsius (10 degree of Celsius temperature variation), which, according to our

model in figure 5.7, we should observe a 2.73 nm shift in SPR peak wavelength [72]. Crude oil temperatures can be up to 150-200 degree of Celsius. Therefore, our fluid change in RI is likely to be the most significant in impacting measurements. As a result, absolute RI change detection would require temperature information and calibrations. However, the SPR approach could be used to identify relative changes in RI measurements (raw crude oil to deposits).

6.3 Inhibitor testing at ramped titration experiments

The SPR absorbance spectra across a range of titrations ratios for neat crude oil and crude oil with inhibitor 5 is shown in Fig. 6.2. We increased the n-heptane-oil ratio from 0.0 (top left panel) to 1 (bottom right panel) gradually as described in the methods section. Before deposition onset (ratio of 0.0 and 0.2) there is no observable difference between the SPR peak wavelength of neat crude oil (dashed) and the SPR peak wavelength of crude oil with 1000 ppm of inhibitor 5 (solid). As asphaltenes start to precipitate and deposit onto the SPR sensor surface (ratio of 0.4) we can see a difference between SPR peak wavelength of neat crude oil and crude oil with inhibitor. The SPR peak difference grows from 6 nm to 8 nm as the crude oil is further diluted with n-heptane (ratio of 0.6-1), which indicates that the inhibitor is altering the deposition rate and the refractive index of the asphaltenes deposition.

Next, we investigated the effect of different inhibitors on deposition onset and deposition rate of asphaltenes from crude oil titrations. For this purpose, we used a neat crude oil sample and five different inhibitors (inhibitor 1–5) to study the process. The results of our experiments are illustrated in Fig. 6.3 and partially confirm our hypothesis. According to Fig. 6.3, each inhibitor showed a deposition onset point between 0.243 and 0.250 n-heptane-oil volume ratio. The inhibitors did not significantly delay

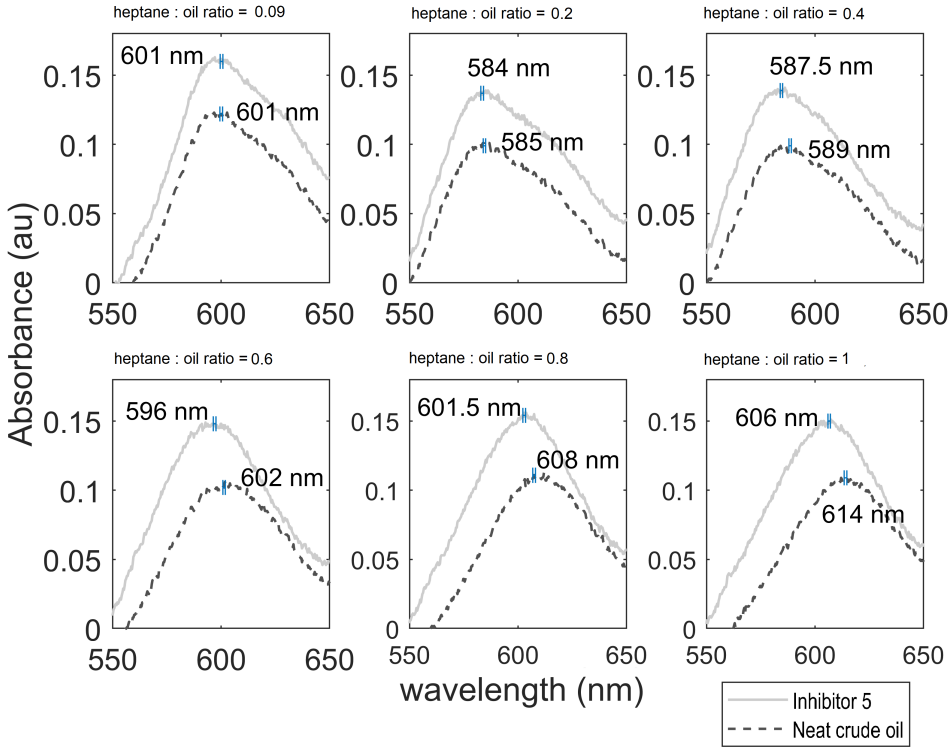

Figure 6.2: SPR absorbance spectra at various heptane-oil ratios for crude oil and crude oil with inhibitor 5 using ramped titration. Blue error bars represent the sensor's typical ± 0.6 nm standard deviation at each peak shown. (For interpretation of the references to color in this figure legend, the reader is referred to the web version of this article.).

the onset point of asphaltene deposition from crude oil using the described setup at these inhibitor concentrations. Further, the resultant SPR peak at onset was within 1 nm for the tested inhibitors, ranging from 583.81 to 584.81 nm. The SPR peak wavelength measured in each inhibitor run showed observable differences after deposition onset. As the heptane-oil volume ratio increased after onset, there was a variance in the slope and the final SPR peak plateau for the different inhibitors. For all runs in Fig. 6.3, the sensing field became saturated with asphaltenes and the SPR peak plateaued after an n-heptane-oil ratio of 0.9. At this stage, the sensor is no longer able to detect further deposition. A plateau at a longer wavelength correlates with a denser deposition. These results indicate that while the inhibitors do not delay the

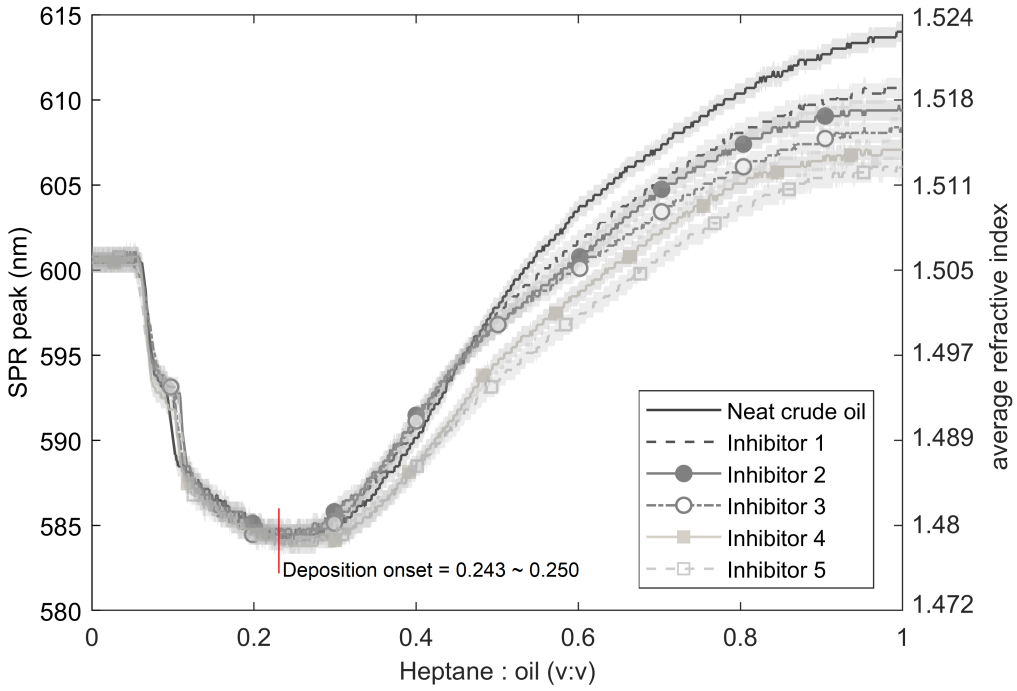

Figure 6.3: SPR peak wavelength and corresponding refractive index for different inhibitors as a function of heptane-oil ratio. Shaded regions represent the sensor's typical ± 0.6 nm standard deviation for each run.

deposition onset with our setup/experimental process, they do affect the characteristics of the asphaltenes formed on the sensor surface. Shaded regions in Fig. 6.3 represent the sensor's typical ± 0.6 nm standard deviation as obtained by triplicate experiments shown in Fig. 5.8 in the Chapter 5. In Fig. 6.3, the average refractive index is shown on the right y-axis using the previously described model. The neat crude oil started the titration experiment with an SPR peak wavelength of 601 nm, which corresponded to a refractive index of 1.504. Similarly, each of the crude oil with inhibitor titration runs also started with a refractive index of 1.504. This measurement reflects the crude oil with asphaltenes still soluble and in the bulk fluid mixture. However, as the titration experiment proceeded and asphaltenes were deposited on the surface, the measured SPR peak showed different final plateaus, depending on the

inhibitor used. Neat crude oil plateaued at 614 nm, corresponding to a refractive index of 1.521. Inhibitors 1, 2, 3, 4 and 5 plateaued at 611 nm, 610 nm, 609 nm, 607 nm and 606 nm-refractive indices of 1.517, 1.516, 1.515, 1.512 and 1.511—, respectively. The deposited asphaltenes on the surface of the sensor has a higher refractive index than neat crude oil due to a higher density, which is reflected in the above values. However, as noted in the modelling section, the deposited asphaltenes will lead to increased absorption when concentrated on the sensing surface than in neat crude oil fluid. If we consider the imaginary part (lossy part) of the refractive index, then the deposit for the neat crude oil that plateaued at 614 nm would correspond to a real component of the refractive index of 1.514. Inhibitors 1, 2, 3, 4 and 5 plateaued at 611 nm, 610 nm, 609 nm, 607 nm and 606 nm would have real components of 1.510, 1.509, 1.508, 1.505 and 1.504—, respectively. To properly distinguish between inhibitors, it would be ideal to have a plateau difference/separation of at least 1.96 times the standard deviation (95% confidence interval). In this case, we can say that differentiating between inhibitors tested in this study would require a separation of 1.2 nm. Therefore, we can note that the profiles from neat crude, inhibitor 1, inhibitor 3 and inhibitor 5 are significantly different. However, inhibitor profile 2 may not be easily distinguished from inhibitor profile 1 or 3. Similarly, inhibitor profile 4 may not be easily distinguishable from inhibitor profile 3 or 5. Therefore, the sensor can differentiate many of the profiles from the range of inhibitors presented, but not all.

6.4 Constant titration comparisons to offline bottle tests

Since the time for asphaltene aggregation in our setup is rather short (∼27 s post-Y-junction), we performed offline bottle tests on neat crude oil to better understand the mechanism behind the formation of the deposit on the SPR sensing surface. We

performed five offline bottle tests, where each of the bottles had a different n-heptane-crude oil ratio; 0.118, 0.194, 0.288, 0.5 and 1. After vigorous mixing, the n-heptane oil mixture was left in the bottle for 72 h to allow for sufficient aggregation [73]. The samples were then agitated to avoid sub-sampling and 5 mL of each mixture was injected at 250 μL/min. The mixture was delivered with a single syringe and the asphaltene deposition monitored using the SPR sensor, results shown in Fig. 6.4A. Interestingly, none of the samples created a deposit over the entire sample injection period. We hypothesized that the asphaltene aggregates grew sufficiently large to prevent adhesion to the sensor surface and hence no deposit was formed or sensed. The SPR peak wavelengths observed can be seen to decrease as the titration ratio increases because the mixture is comprised of more n-heptane (lower refractive index). We investigated the size of the asphaltene particles with microscopy to confirm that the SPR sensor showed a sensitivity to flocculate size.

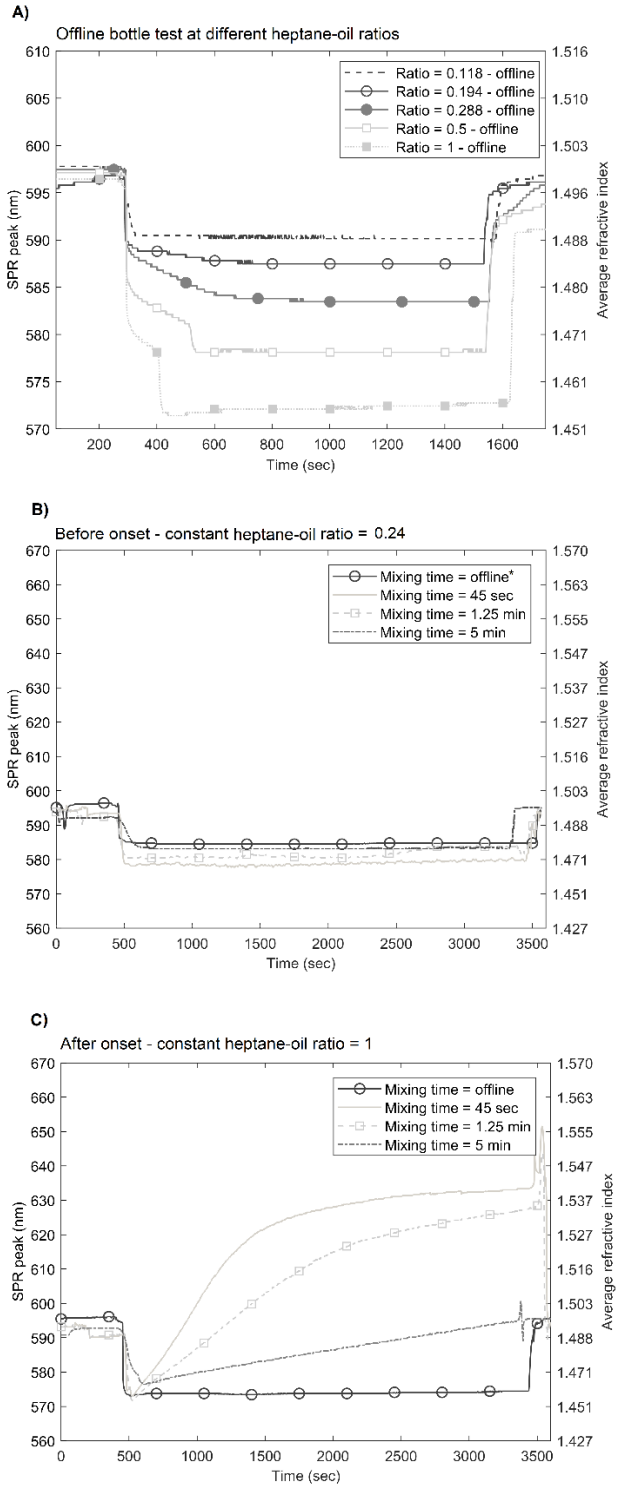

Figure 6.4: SPR peak wavelength as a function of time for (A) bottle tests of different heptane-oil ratios, (B) before deposition onset for different mixing times and (C) after deposition onset for different mixing times. *Offline bottle test at volume ratio of 0.194 to compare with the online test volume ratio of 0.24 in (B).

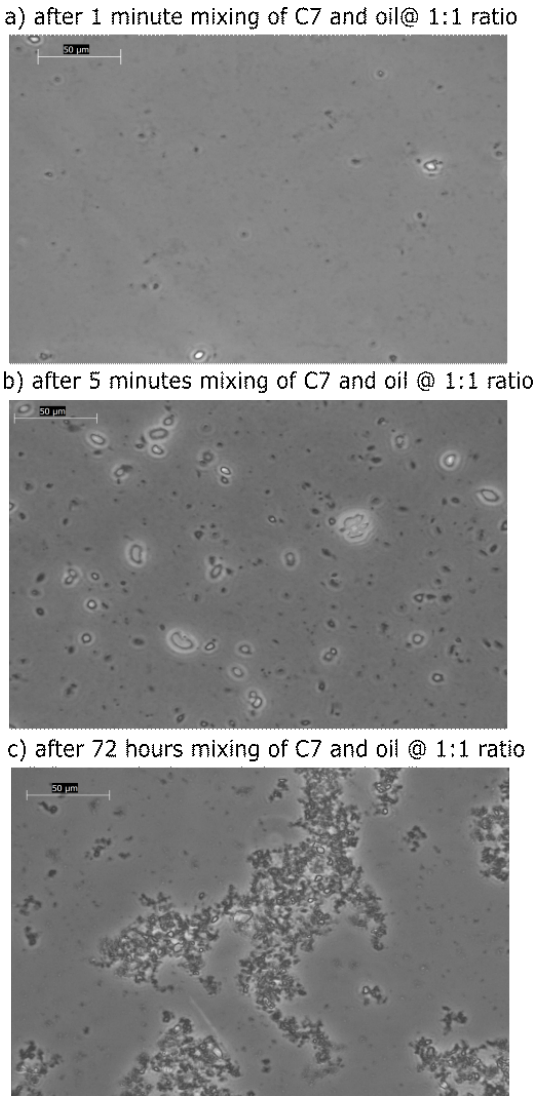

Figure 6.5: Microscopic photos taken from 1:1 ratio of heptane and crude oil with different mixing times, a) after 1 minutes of mixing, b) after 5 minutes of mixing and c) after 72 hours. Note that scale bar at top left shows 50 μm.

Fig. 6.5 shows that as we increased the incubation time from 1 min to 72 h at a volumetric ratio of 1:1, asphaltene aggregates grew and formed islands. At 1 min, very few aggregates reached 1 µm to be observable by visual microscopy, but there were a few detected. At 5 min, several aggregates were observed in the several micrometer size range. At 72 h, islands of asphaltenes were detected that spanned several hundred microns. The microscopy data aligns well with our inability to detect shifts in the

SPR peak wavelength when we used offline oil and heptane mixtures aged for 72 h. It appears that the large aggregates of asphaltenes do not deposit and/or accumulate to be readily sensed within the 100-300 nm penetration depth of the SPR field. These results inspired us to look at different post-mixing residence times with our online titration approach. For testing the impact of mixing residence time, we changed the output tubing line length to achieve different post-Y-junction transit times of 5 min, 1.25 min, and 45 s. We executed a single fixed titration ratio instead of a ramped titration of changing ratios, and we reduced the combined flowrate from 250 $\mu L/min$ down to 100 $\mu L/min$ to allow for longer mixing times. The corresponding lengths of line were 1100 mm (502 μL), 275 mm (125 μL) and 165 mm (75 μL) of 0.762 mm I.D FEP tubing, respectively. Two experiments were performed at heptane-oil volume ratio of 0.24 or before onset as shown in Fig. 6.4B, and at an n-heptane-oil volume ratio of 1 or substantially after onset as shown in Fig. 6.4C. The volume ratio is calculated as flow rate of n-heptane divided by flow rate of crude oil; for example, 0.0194 μL/min $\div$ 0.0806 μL/min equates to 0.24. For Fig. 6.4B, this equated to flowrates of 0.0194 μL/min for n-heptane and 0.0806 μL/ for crude oil, while for Fig. 6.4C both flowrates were set to 0.05 μ L/min. Each run included a n-heptane, toluene, and oil sample flush prior to the titration process. Fig. 6.4B and 6.4C indicate that the transit mixing time greatly impacts the SPR sensor response after asphaltene deposition onset. In Fig. 6.4B at a volume ratio of 0.24, or "just" before deposition onset as is practical with these flow rates based on our pumps and syringes, as expected, there is no asphaltene deposition since there is not enough n-heptane to induce asphaltene precipitation. However, after deposition onset, as shown in Fig. 6.4C, there are noticeable differences between the SPR profiles with various mixing times. As the transit time decreased from 5 min to 45 s, the deposition rate increased dramatically. With a 45 s mixing time, the SPR peak wavelength rapidly climbs from an initial value of $\sim$570 nm to a plateau of $\sim$635 nm indicating rapid

deposit formation. Further, with a fixed titration ratio of 1, we observe a higher ∼635 nm SPR peak plateau Fig. 6.4C compared to the ∼615 nm plateau observed in Fig. 6.3 when a ramped titration was performed. We attribute this difference to signify that a subfraction of asphaltenes are precipitated in the ramped ratio titration compared to the constant ratio titration. The ramped titration slowly induces the most unstable subfraction of asphaltenes to precipitate and deposit, while at a fixed ratio we are inducing a larger portion or subfraction of asphaltenes to precipitate and deposit. This alters the composition of the deposit on the metallic thin-film and could eventually be used for asphaltene distribution studies. Conversely, when the mixing time is increased to 5 min, the SPR peak slowly increases (almost linearly) from ∼ 570 nm to 595 nm and never reaches a plateau.

6.5 Mechanism validation tests

We hypothesize that the shorter mixing times produce smaller asphaltene aggregates, which may facilitate the attachment of asphaltenes to the thin metal-film or SPR sensing surface. Similarly, with the longer mixing times, an increasing amount of larger aggregates are formed, slowing the attachment to the metal sensing film and deposition. We conducted SPR measurements of known condensed phase material, both n-heptane and n-pentane asphaltenes, to test our theory that a subfraction of asphaltenes were deposited during a ramped titration (∼615 nm plateau) compared to the constant 1:1 titration (∼635 nm plateau). Asphaltenes were precipitated at a volumetric ratio of 40:1 titrant to crude oil sample and left to incubate for 72 h. The maltenes were removed and the asphaltenes at the bottom of the vial were transferred to the SPR sensor, configured differently than described above. Instead of sensing a sample from the top of the flowline, the SPR sensor was flipped around so that the sensing surface was at the bottom of the fluid sample. A 3D-printed holder

was created to provide a chamber for batch loading/containment of the sample. The asphaltenes solution was introduced to the gold surface and the excess precipitant was allowed to evaporate, forcing or pushing the asphaltenes to the sensing surface. A microscope image of the n-pentane asphaltene solution is shown in Fig. 6.6. Fig.

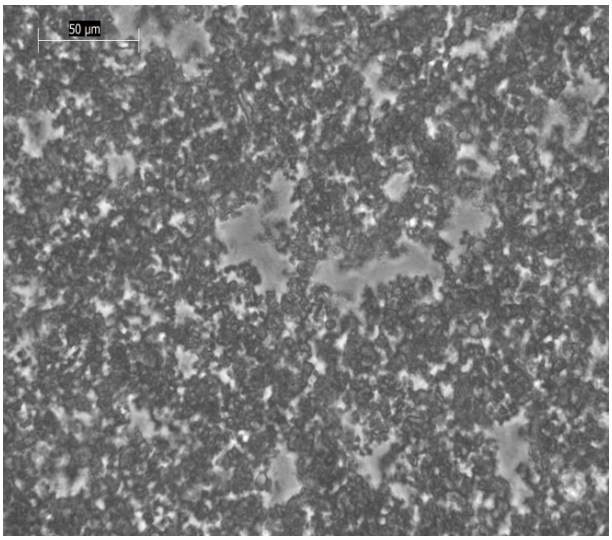

Figure 6.6: Microscopic photo of 40:1 volume ratio of mixture of pentane and crude oil. Note that the scale bar at top left shows 50 μm.

6.7 shows the data acquired by positioning the SPR sensor surface at the bottom of the sample fluid, instead of the top of the flowline as is typical. In Fig. 6.7A, the SPR peak wavelength versus time is shown for the duration of evaporation. Over time, the n-pentane and n-heptane evaporates and gradually "deposits/pushes" the respective asphaltene flocculates toward the SPR sensor surface. It can be observed that the SPR peak for n-pentane rises more rapidly than n-heptane, as expected. No SPR signal shift was observed when the chamber was covered with a glass coverslip and evaporation was prevented, dataset labelled "C7 with cover". Fig. 6.7B is a series of photographs of the SPR sampling chamber over time for the C7 dataset for the first 29 min. Initially, the gold surface is covered with n-heptane asphaltene solution and evaporation starts concentrating the flocculates, labelled stage I. Next, gravitational settling occurs in stages II and III, visualized by the pattern that emerges on the

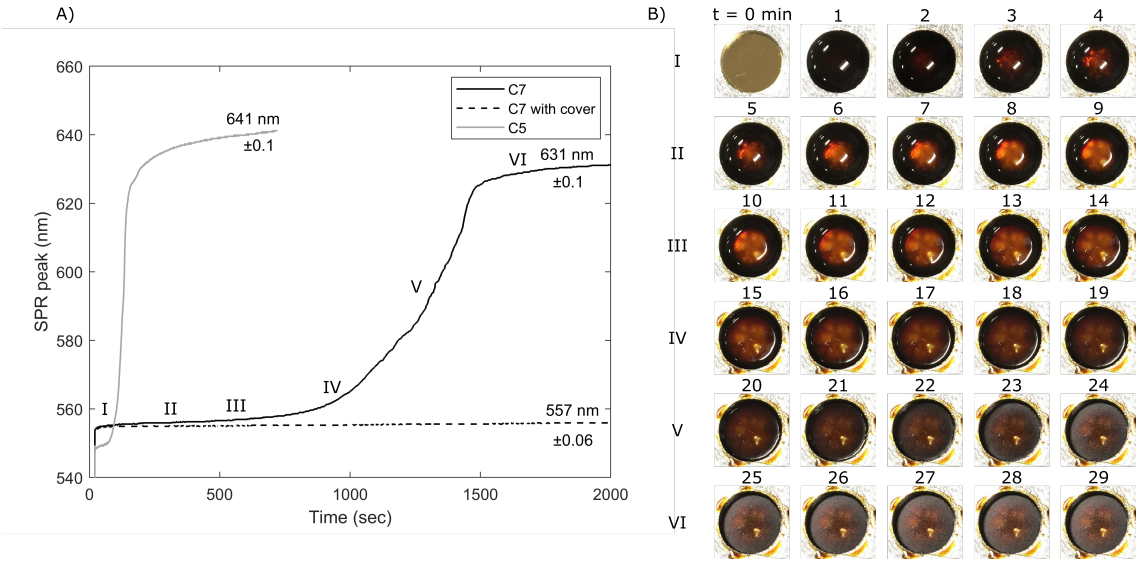

Figure 6.7: Data acquired positioning the SPR sensor surface at the bottom of the sample fluid, instead of the top of the flowline as is typical. A) SPR peak wavelength versus time for the evaporation tests described in the text. N-heptane (C7) and n-pentane (C5) asphaltenes were precipitated at a volumetric ratio of 40:1, maltenes were removed, and the asphaltenes transferred into the sample chamber. Over time, the excess C5/C7 evaporates and gradually "deposits/pushes" the asphaltene flocculates toward the SPR sensor surface, except for the dataset labelled "C7 with cover", in which a coverslip prevented evaporation. B) Photographs of the SPR sampling chamber over time for the C7 dataset for the first 29 min. Initially, the gold surface is covered with C7 asphaltene flocculates suspended in n-heptane, labelled stage I. Next, gravitational settling occurs in stages II and III as visualized by the pattern that emerges on the gold surface, noting a negligible shift in SPR peak wavelength. The n-heptane continues to evaporate in stages IV and V, to the point that a matte finish can be observed with minimal surrounding fluid, noting a climbing SPR peak wavelength. Finally, in stage VI, there is minor visual change, which is in agreement with the SPR signal plateau observed.

gold surface. The n-heptane continues to evaporate in stages IV and V, to the point that a matte finish can be observed with minimal surrounding fluid. Finally, in stage VI, there is minor visual change, in agreement with the SPR signal plateau observed. There are two main points to be made from the data in Fig. 6.7. First, the plateau of n-pentane asphaltenes (∼641 nm) is higher than the SPR plateau of n-heptane asphaltenes (∼631 nm), confirming that the sensor can detect variations in the asphaltene deposit density and composition. The n-heptane asphaltenes in

excess precipitant, 40:1, result in an SPR signal of 631 nm that is close to SPR signal at 635 nm observed in Fig. 6.4C at a 1:1 ratio. The lower SPR plateau of 615 nm from a gradual titration, Fig. 6.3, suggests that the SPR sensing field is filled with a less dense sub-fraction of asphaltenes. Second, it is important to note that the excess precipitant, 40:1, C7 asphaltenes are not detected by the SPR approach without evaporation. Even with adequate time for gravitational settling, there is no SPR signal shift noted in Fig. 6.7 with a relatively flat profile at 557 nm, close to n-heptane at 553 nm. This suggests that the asphaltene flocculates, tens to hundreds of microns, remain outside the penetration depth of the SPR field of 100-300 nm. Not until they are "pushed" into the SPR probe region are they detected as shown by the other datasets in Fig. 6.7. The above evaporation study coupled with visual microscopy indicate that the SPR sensor is highly sensitive to sub-micron particles and depositions. Larger micron-sized flocculates that are flowing past the sensor, or that are sufficiently suspended beyond the penetration depth, will not be readily sensed. The data indicates SPR can be used for detecting changes in the initial sub-micron asphaltene deposition events, including when altered by inhibitors. Instead of ramped titrations (data like that in Figs. 6.2 and 6.3), we investigated the impact of an inhibitor on asphaltene deposition at a fixed titration ratio for extended times (procedure and data like that in Fig. 6.4). Also, we study the effect of inhibitors on asphaltene deposition from crude oil while tracking the deposition peak and the fluid peak separately using a two peak model function at different n-heptane-oil ratios. When asphaltenes begin to precipitate and deposit from the crude oil, a subtle second peak appears in the absorbance curve using the SPR sensor. This second peak is associated with the asphaltene deposited layer in the sensing field. The asphaltenes that begin to form and are measured by the sensor are much denser than the n-heptane-oil mixture in the line and therefore have a resonance frequency lower (therefore longer wavelength) than the mixture. We can therefore expect that

a good inhibitor decreases the SPR peak wavelength of asphaltene deposited layer. Fig. 6.8 compares the SPR absorbance spectra for neat crude oil (black dashed lines)

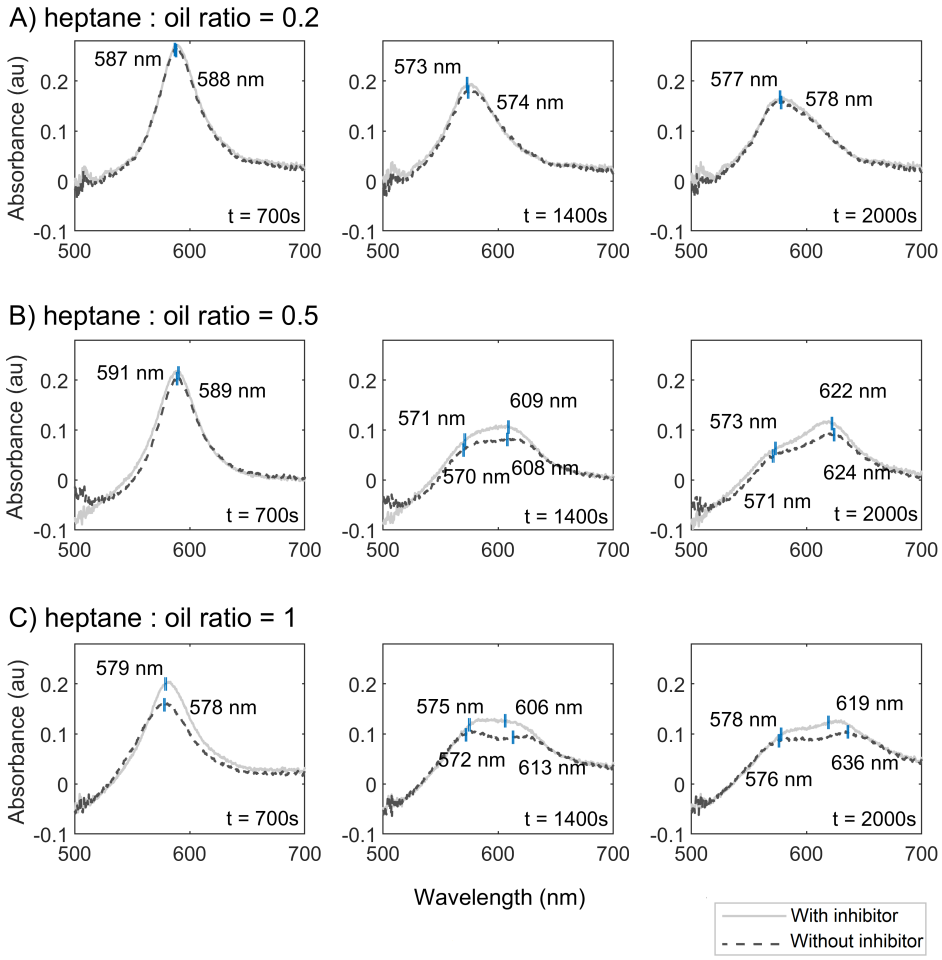

Figure 6.8: SPR absorbance spectra for crude oil and inhibitor 5 in a constant ratio experiment at (A) heptane-oil ratio=0.2, (B) heptane-oil ratio=0.5 and (C) heptane-oil ratio = 1. The first column corresponds to 700 s, second column correspond to 1400 s and third column correspond to 2000 s. Blue error bars represent the sensor's typical ±0.6 nm standard deviation at each peak shown. (For interpretation of the references to color in this figure legend, the reader is referred to the web version of this article.)

against crude oil with inhibitor 5 (grey solid lines) at constant titration ratios. Three experiments where conducted with fixed n-heptane-oil ratios of 0.2 (Fig. 6.8A), 0.5 (Fig. 6.8B) and 1 (Fig. 6.8C). For each experiment, we plot the SPR absorbance

spectra at three time frames: t = 700 s or the left plot that indicates the initial mixing of n-heptane with crude oil sample, t = 1400 s or the middle plot that indicates the region of forming the deposit, and t = 2000 s or the right plot that indicates the region of plateau or sensor saturation (similar to Fig. 6.8C). As expected, Fig. 6.8A shows that before onset (ratio of 0.2) the SPR spectra and peak wavelength of crude oil is similar to crude oil with inhibitor at all three times (i.e. no deposition). In Fig. 6.8B and Fig. 6.8C, we observe a second peak in the absorbance spectra for t = 1400 s and t = 2000 s, which shows the deposition dynamics over time. At t = 700 s, there is only a single peak in either Fig. 6.8B or 6.8C left panels, as this is the start of the titration run where the n-heptane and crude oil are initially mixed. At 1400 s, we can see the introduction of a second peak, or the asphaltene deposition peak in both Fig. 6.8B and C. In Fig. 6.8B middle panel, at a ratio of 0.5, the crude oil with inhibitor and the neat crude oil show little difference with the deposition peak at $\sim$ 608 nm. In Fig. 6.8C middle panel, at a ratio of 1, the crude oil with inhibitor is lowering the deposition peak (606 nm) compared to the neat crude oil deposition peak (613 nm). The trend of lowering the refractive index of the deposit continues until the sensor saturation at t > 2000 s. In Fig. 6.8B right panel we see a gradual reduction in the refractive index / SPR peak, down from 624 nm (neat) to 622 nm (inhibitor). In Fig. 6.8C right panel, we see a more notable reduction from 636 nm (neat) to 619 nm (inhibitor). In both right panels of Fig. 6.8B and 6.8C, we also note that the second peak (deposit) is now larger (more absorption) than the first peak (fluid) in the saturation region. Fig. 6.9 is a plot of the dual SPR peak wavelengths versus time, extracted from the same experimental data used for Fig. 6.8B and C. Fig. 6.9A shows the n-heptane-oil volume ratio of 0.5 and Fig. 6.9B shows the n-heptane- oil volume ratio of 1. The data shown in Fig. 6.9 highlights that the deposition SPR peak wavelength (second peak in the spectra analysis, Fig. 6.8B and C) is much longer than the fluid SPR peak wavelength (first peak in spectra, Fig. 6. 8B and C). In all cases, the fluid peak

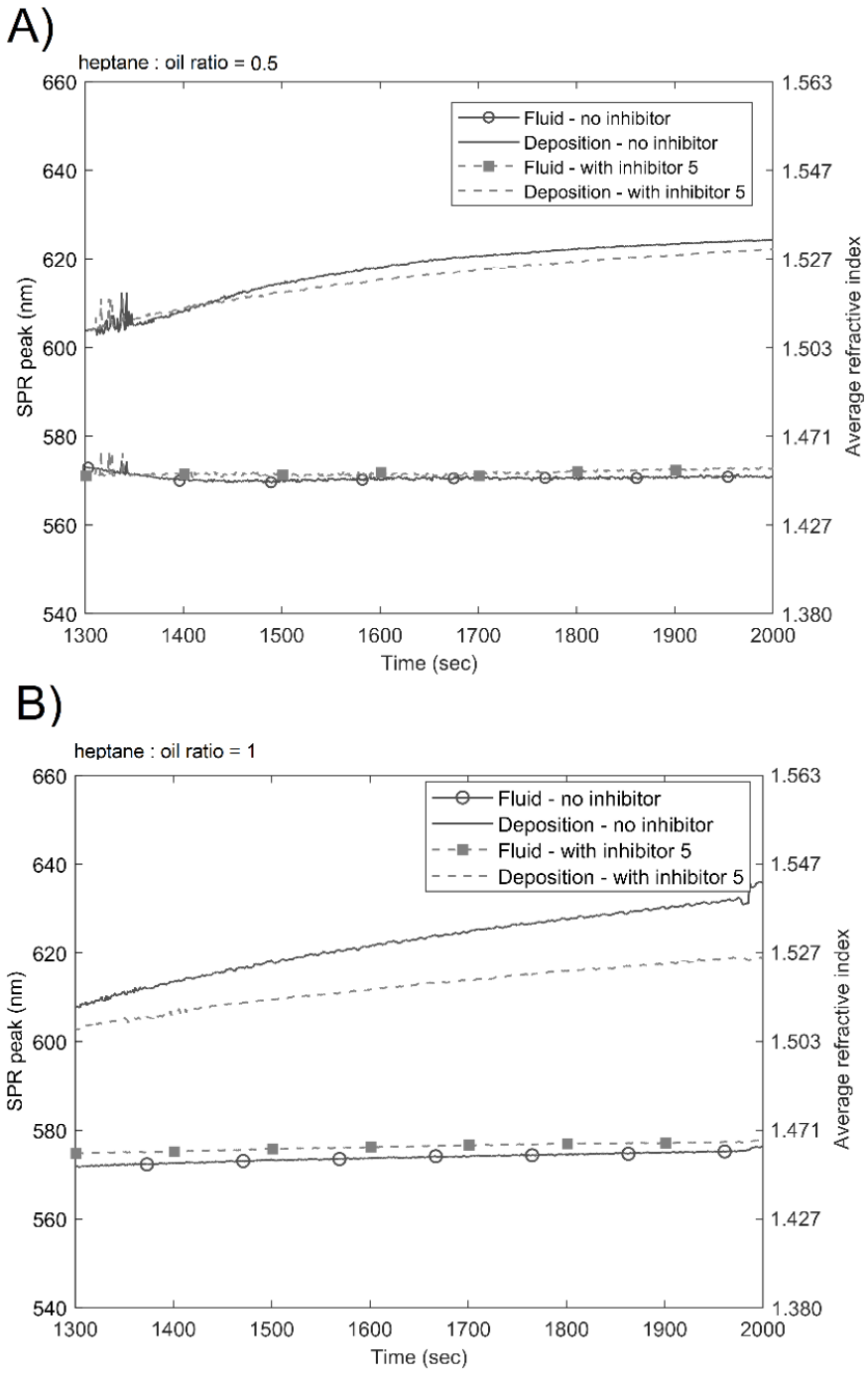

Figure 6.9: SPR peak wavelengths and corresponding refractive index for crude oil (with and without inhibitor) for the fluid and the deposit when the spectral data are analyzed with a two peak model function.

remains relatively constant at 570-580 nm. For both ratios, the inhibitor is effective at reducing the SPR peak wavelength, or the deposit's refractive index, but more so for the heptane-oil volume ratio of 1 in Fig. 6. 9B. We can also see that deposition rate (SPR peak wavelength change versus time) reduces by adding inhibitor to the crude oil sample. The final deposition refractive index was also lowered from 1.545 to 1.527 when mapping to a real component only refractive index and 1.540 to 1.520 when considering the complete complex refractive index. In the constant flow-rate data shown in Figs. 6.8 and 6.9, as the experiment proceeds, we propose that less of the fluid component is sensed (lower SPR peak) and more deposited asphaltenes are sensed (higher SPR peak). The lower SPR peak wavelength stays relatively constant as the fluid composition throughout the experiment remains unchanged due to replenishment of the crude oil and n-heptane mixture supplied by the syringes. The amplitude of the lower peak decreases since less of the fluid is being interrogated over time as the deposit grows. Conversely, the higher SPR peak from the asphaltenes increases in wavelength, as the composition of the ever-growing deposit may shift to include heavier molecules after the initial seeding layer. Further, the amplitude of the higher SPR peak also increases, suggesting a greater extent of the sensing field is filled by the deposited asphaltenes. Our modelling efforts in the Chapter 4 closely agree with this two-component system and will be expanded upon in future work. Collectively, our findings highlight the useful data gathered from SPR sensors for the screening and selecting of asphaltene deposition inhibitors. In summary, we demonstrated that a wavelength interrogation mode surface plasmon resonance (SPR) sensor can be used to study and compare crude oil asphaltene chemical inhibitors. We have shown that shifts in the peak SPR wavelength can be used to identify the onset of deposition, the rate of deposition, and the final refractive index of the deposit from a titration experiment. We evaluated multiple inhibitors and showed that SPR peak wavelength can be used to directly measure the asphaltene deposition. In a screening

method or workflow, the original neat crude oil would be run first to establish a "blank" or comparative control run. Then, subsequent experiments combining crude oil with various inhibitors at various concentrations would be performed on the senor to provide meaningful data on the effectiveness in slowing or changing the deposited material. Future studies may utilize the SPR sensing technique to perform asphaltene inhibitor screening at reservoir conditions. In the next chapter, we will study the application of the wavelength interrogation mode SPR sensor in dentistry.

Chapter 7

Application of SPR sensor in dentistry

In this chapter, we study the SPR peak variations of resin composite before and after curing with UV light. The results presented in this chapter are first steps towards understanding the optical properties and refractive index of dental resin composites. Here we aim to understand the effect of illumination distance and time on the variation of SPR peak and refractive index of resin during UV curation.

7.1 Background and motivation

Resin composites are used regularly as the filling materials for teeth in dentistry as adhesive restorative materials [74]. The most reliable feature of dental resin composite is the micro-mechanical retention property which makes filling the small cavities (teeth) more effective [74, 75]. There are different types of dental resin composites with different physical, chemical and optical properties [76]. The different properties are due to unique concentrations of each component in the synthesis process of resin composites [76, 77]. The composite curing are strongly influenced by the type and amount of photo-initiators inside the material [76]. Therefore, different resin based composites require different light energy levels for proper curing which is an important issue in dentistry [74]. One of the methods of analyzing the curing process of resin composite is the color [76]. The resin composite restorations can result in a grayish shade depending on the composite material [76] . Therefore, successful restoration of

resin composite was predicted using the color and translucency before and after curing with light source [76]. Curing process not only affect color of resin composite, but also affect the refractive index of the composite material [76]. As the curing process depends on the average magnitude of refractive index change in the resin material before and after curing with light source, one can employ a refractive index sensor to understand how resin properties will be evolved during the curing process. Surface plasmon resonance (SPR) sensors are novel instruments for detecting the change in refractive index of different materials with high accuracy and in real-time [11, 38, 78]. The aim of this study is to evaluate the dental resin composites refractive index before and after curing using an SPR sensor. We first show that how a change in SPR peak wavelength corresponds to a change in resin composite refractive index. Then, we study the resin composite curing process using SPR sensor and investigate the role of illumination time, UV light distance and composite material in curing process of dental resin.

7.2 SPR Sensor and materials

7.2.1 Resin composites

The dental resin composites used in our experiments were Filtek Supreme manufactured by 3M ESPE with a code shade of Enamel provided by BlueLight Analytics. The fillers of the resin composite are a combination of a non-agglomerated/non-aggregated 20 nm silica filler, a nonagglomerated/ non-aggregated 4 to 11 nm zirconia filler and an aggregated zirconia/silica cluster filler (comprised of 20 nm silica and 4 to 11 nm zirconia particles). This filler was custom molded to a well-defined size using a stainless-steel, split plate with a 2 mm thicknesses and hole diameter of 7.2 mm was used as the molds to produce standardized specimens. The model was filled

with resin composite material and covered with clear celluloid strips on the top of the hole.

7.2.2 SPR sensor setup

In this study, the Kretschmann configuration which is a reliable setup of the SPR sensing has been used to detect the variations in resin composites. The setup of Kretschmann configuration was reported in the previous chapters. The setup has been slightly modified to be used for sensing dental resin composite.

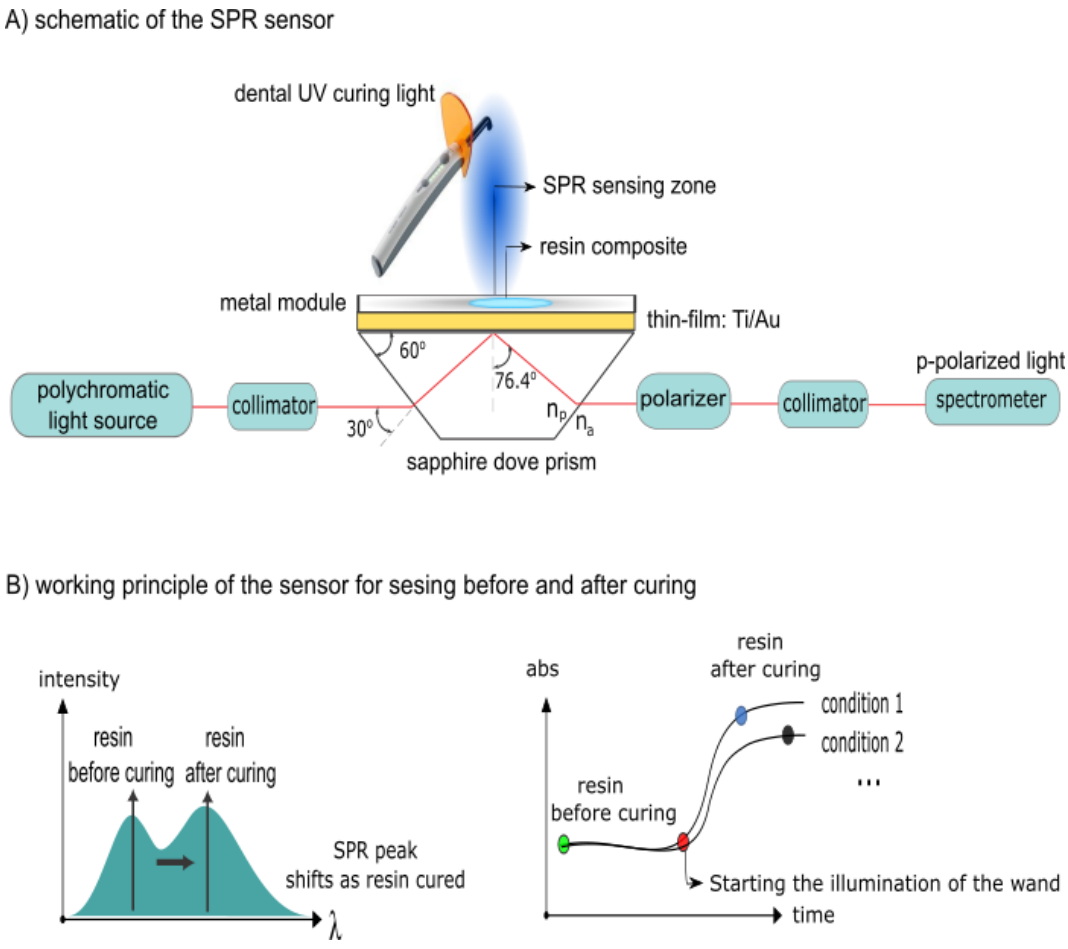

Figure 7.1: (A) Schematic diagram of the experimental setup and (B) concept of SPR sensor for measuring the dental composite resin before and after curing at different conditions.

As seen in Fig. 7.1A, the prism has been flipped in order to cure the resin using UV light. We fabricated a holder to keep the sensor secure as the resin in injected from the top by using the 3D-printer. Fig. 7.1B shows the working principle for dental based resin composite before and after curing. At the beginning of the experiment, the sensing area is filled with uncured resin. When the illumination starts (using the UV wand), the SPR peak shifts towards the longer wavelength as cured resin have higher density. As the resin start to cure, its refractive index (RI) start to increase over time. Even after turning off the wand, the RI still increases as the resin continue to cure itself (post curing phenomenon). To record and analyse the data, a custom LabView program which was discussed in Chapter 5 has been used. The Light curing unit (wand) used in the experiments is Elipar DeepCure STM. This is an LED curing light with a utilizable wavelength range of 430 – 480 nm and a peak wavelength of 450 nm. The curing unit has an intensity of 1470 mW/cm^2 and a tip diameter of 8.8 mm. The UV wand intensity as a function of illumination distance is illustrated in Fig. 7.2. The UV wand intensities between 0 and 10 mm has been obtained from the instrument data sheet (blue points). For longer distances, the light intensity was measured by a power meter through the metal ring at 10, 20, 30, 40, and 50 mm illumination distances (red points). According to the data, the intensity of UV wand decays rapidly as illumination distance increases. We also developed a theoretical model by considering the source illumination as a cone where the illumination area increases by an increase in illumination distance. In the model, the divergence of the cone is assumed to be 10 degrees. According to this model, the intensity decreases by squared of the radius of illumination area. Fig. 7.2 demonstrate the agreement between the theoretical model and measured intensities. The thickness of deposited resin composite in the sample position during the experiments was around 2 mm. Therefore, the epoxy is approximately 10,000 times thicker than penetration depth of the sensor (100 - 300 nm). It should be noted that while UV wand cured the resin

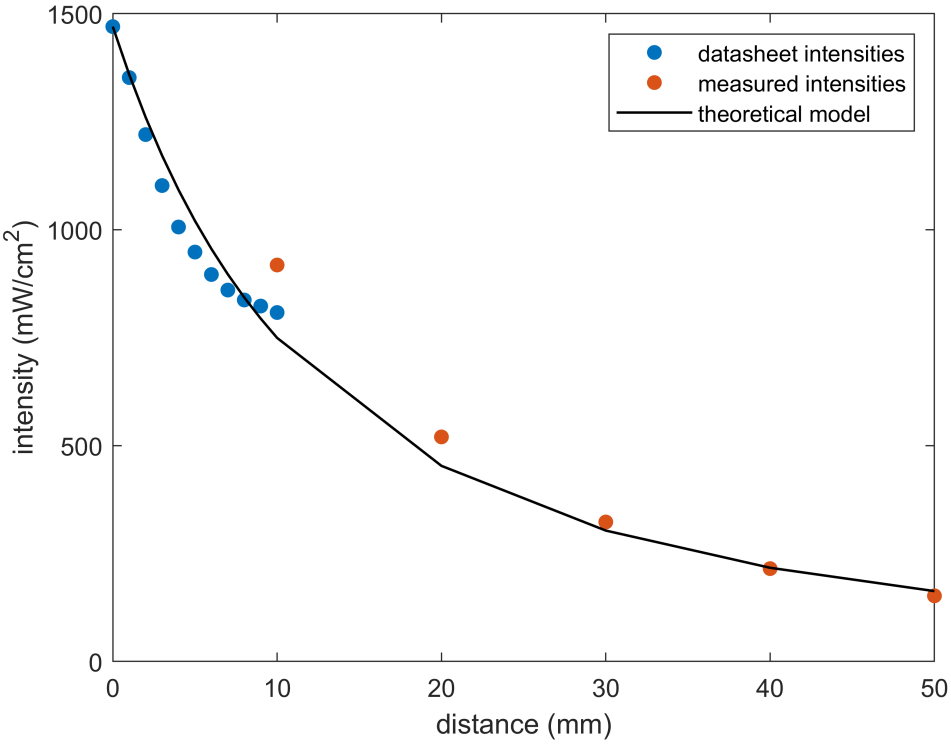

Figure 7.2: UV wand intensity as a function of illumination distance. Note that the blue points are the intensities obtained from datasheet of the wand, red point are measured intensities through the metal ring, and black line is the theoretical model.

sample from the top, we sensed the sample from the bottom (the other side). The highest UV light intensity is on the surface of the resin while the UV intensity drops as light is attenuated deep through the sample. This means that we are sensing the sample on the least cured side. If the thickness of the filling/holder is changed (i.e. depth of sample) this will change the final intensity that we are measuring with SPR.

7.3 Varying UV-exposure time measurements

To show the repeatability and the reliability of the sensor, we conduct the triplicate runs. The three different runs using the same dental resin material are mostly the

same and the error of the experiment is less than 1 nm which is within the spectrometers' wavelength resolvability. The resin had been injected into the sensing zone of the sensor and remained in the sample position for 170 seconds without UV curing. As seen in Fig. 7.3, the SPR peak of the resin for each run before curing is the same (≈ 617 in three runs). The curing process of the dental resin had been started when the

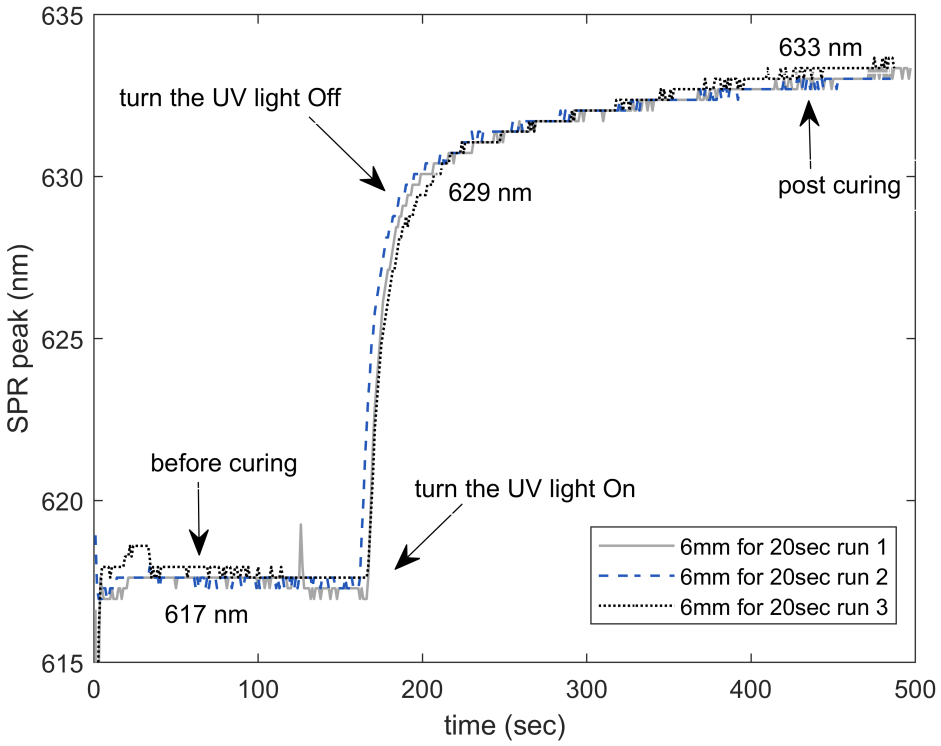

Figure 7.3: Triplicate runs of resin before and after curing at 6mm distance of the wand and SPR sensing zone for 20 seconds of illumination to show the repeatability of the results for the sensor.

wand turned on (at 170 second). As a result, the SPR peak shift towards the longer wavelength from ≈ 617 nm to ≈ 630 nm. The illumination time in this experiment was 20 seconds. As seen in the Fig. 7.3, the SPR peak continued to increase even after turning off the wand. This process is called post curing of the dental resin which took place for almost 310 seconds. we observe that, the refractive index of the dental resin composite increases after curing by hardening itself. To understand the effect of

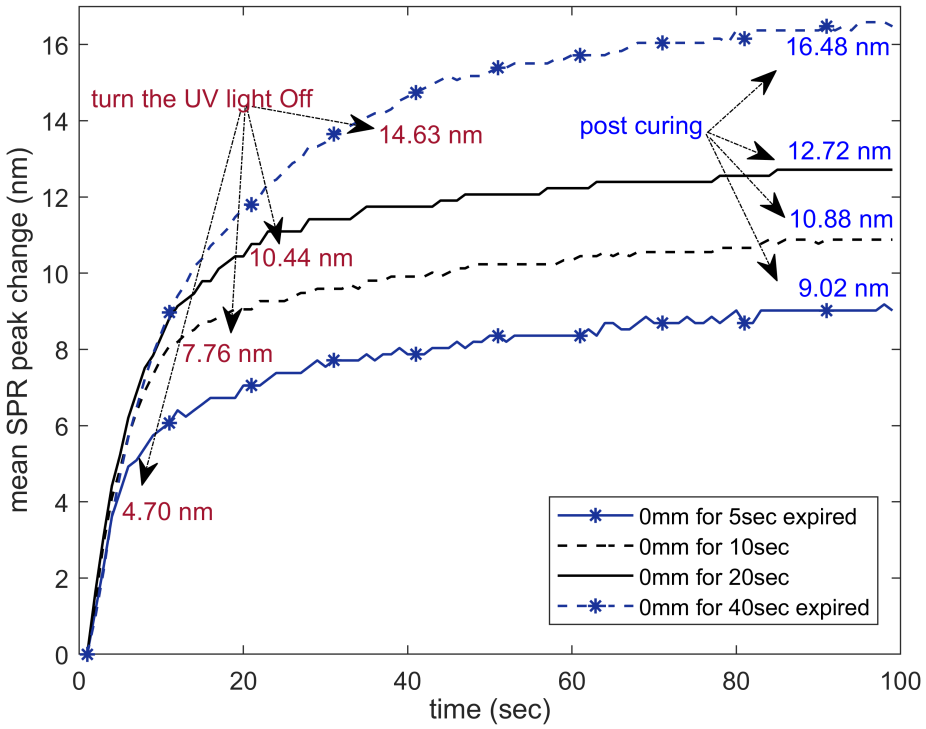

Figure 7.4: Mean SPR peak change as a function of time at different illumination time of wand at same distance. Note that all the runs here are an average of three runs.

illumination time for curing the dental resin composite, we performed another series of the experiments. For this purpose, we conduct four different runs at same distance (0 mm) between the wand and the resin at four different illumination times. The illumination times are 5, 10, 20, and 40 seconds. Please note that each of these data sets are the average of three runs. To clearly show the impact of varying the illumination time, we recorded and analyzed the SPR peak wavelength versus time. As Fig. 7.4 demonstrated, the mean change of the SPR peak increases by increasing the illumination time. The red values are representing the values of the mean change of the SPR peak of dental resin composite after turning the UV light off. Also, the blue values are corresponding to the post curing values of the mean change of the SPR peak.

7.4 Varying illumination distance measurements

Fig. 7.5 shows the result of the other series of measurements on the curing dental resin composite. Here, we investigated the effect of the distance between the wand and the sensing zone on resin curing. Note that all the data sets are the average of the three different runs at the same illumination time with the same material. The illumination time were same for all the runs while the experiment took place at the 0, 20, and 50 mm distance between the wand and the sensing zone. From Fig. 7.5 it is clear that by increasing the distance between the wand and the sensing zone, the mean change of the SPR peak decreases which can be due to lower energy transfer from wand to the resin composites (more loss).

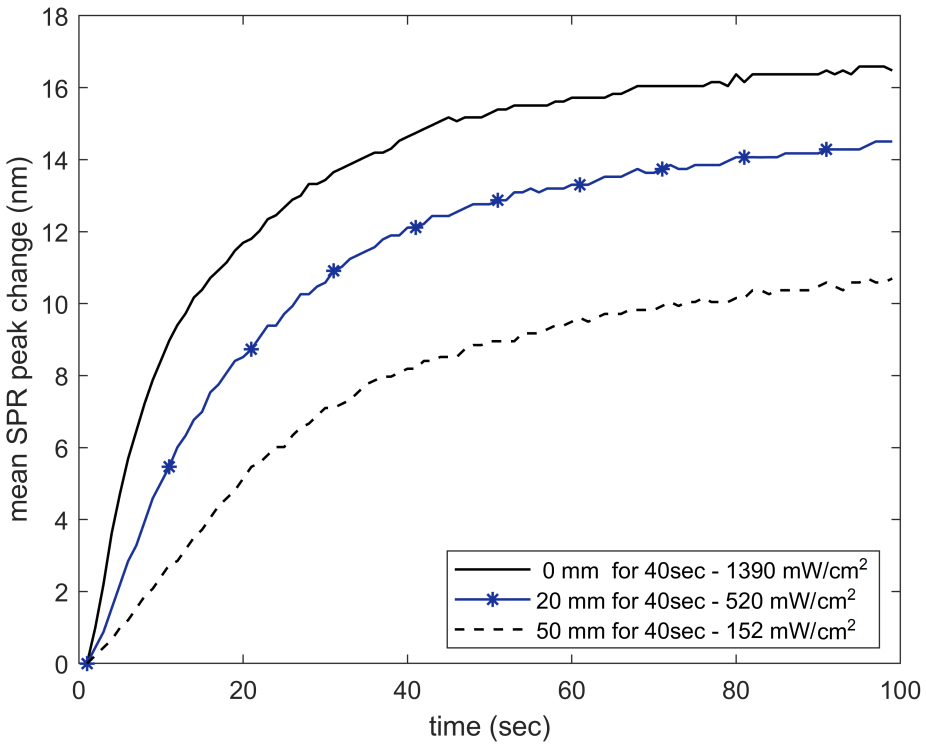

Figure 7.5: Mean SPR peak change as a function of time at different distance between wand and SPR sensing zone. Note that all the resin in this figure are expired resins. Each run here is an average of three runs.

Fig. 7.6 illustrates the SPR absorbance spectra of resin composite before and after curing with UV wand. The absorption spectra of resin before curing is demonstrated

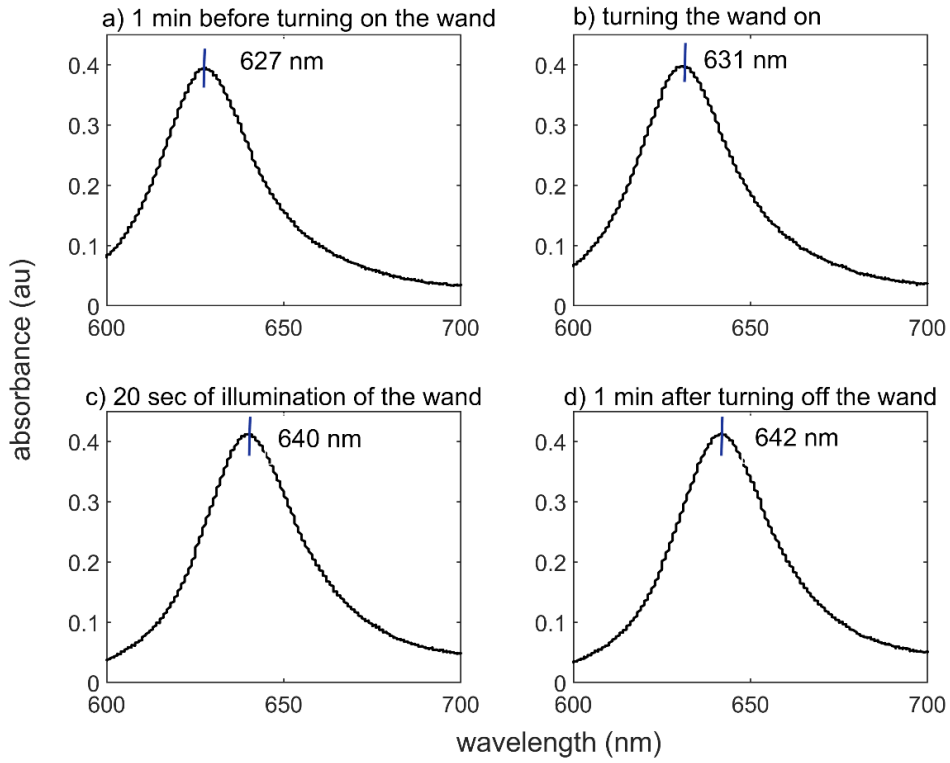

Figure 7.6: SPR absorbance spectra of resin before and after curing. a) one minute before turning the wand on. b) at the time we turn the wand on. c) after 20 seconds of illumination of the wand. d) one minute after turning the wand off.

in Fig. 7.6(a) with a peak value at 627 nm. As seen in Fig. 7.6(b) as we turn on the UV wand the absorption peak shifts toward longer wavelength (631 nm) which means dental resin composite is curing. After 20 second of UV illumination in Fig. 7.6(c), the absorption peak shifts significantly to longer wavelength (640 nm). By turning off the UV wand (Fig. 7.6d), absorption peak still shifts slightly (to 642 nm) due to post curing process (hardening of resin composite).

Chapter 8

Conclusion and future directions

In this thesis, different applications of prism-based SPR sensors for detection of phase changes in opaque materials have been studied. We proposed a prism-based Kretschmann configuration of SPR sensor for monitoring the refractive index changes in opaque materials in real-time and with an easy setup. We modelled our sensor using the matrix method and calibrated with well-studied and known solvent combinations and showed excellent agreement between theoretical predictions and experimental results. The operational range of our wavelength interrogation mode SPR sensor enable measurement of an SPR peak wavelength from 553 nm to 695 nm (142 nm) which is equal to 0.197 change in refractive index (RI) from 1.389 to 1.586. Using the SPR sensor, two specific applications were explored in detail. First, monitoring asphaltene deposition in crude oil and the effects of inhibitors on the asphaltene deposition have been studied. Second, the effect of UV light, including UV exposure time and illumination distance, on curing of the dental resin composite have been investigated in detail. In the first application, we showed that inhibitors can signifcantly reduce the asphaltene deposition rate and depth in crude oil. For the second application, we demonstrated that the UV exposure time and illumination distance are important in quality of resin curing in dentistry applications. We showed that crude oil RI varies from a RI value of 1.505 (SPR peak wavelength of 601 nm) in neat crude oil fluid to a RI value of 1.521 (SPR peak wavelength of 614 nm) when asphaltenes deposited on the surface of the sensor completely. In dental application, we similarly show that

resin composite SPR peak wavelength shifts from 617 nm before UV curing to 633 nm after a complete UV curing. We demonstrated that SPR sensors can be used in similar application for real-time monitoring of phase changes and different physical and chemical properties of opaque materials.

Future directions that continue the work of this thesis are enumerated below:

1. The dental resin project requires that a hardness test [American Society for Testing and Materials (ASTM)] be performed on resin composite, and compare the resin hardness under different illuminations with the optical wavelength shift observed in the experiments. The particular standard for the experiment should be ASTM D785-08. The ASTM Rockwell Hardness test is a hardness measurement based on the net increase in depth of impression as a load is applied [79]. In the experiments, the resin composite should be placed on the surface of the Rockwell Hardness tester. Then, a minor load is applied and the gauge is set to zero (calibration). Finally, the major load is applied and after 15 seconds the major load is removed [79]. The resin composite should be allowed to recover for about 15 seconds and then the hardness can be recorded from the dial while the minor load still applied [79]. To understand the effect of UV curing on the hardness of resin, the conditions of these experiments should be exactly similar to the ones presented in Chapter 7 when UV wand is off, and when UV wand is on (with different illumination times and distances).

2. We need to apply the Matrix method proven to work for our crude oil analysis and adapt to the Dental materials and setup. This can help to easily relate the SPR peak wavelength from experiments to RI of resin during UV curing.

3. In the asphaltene project we should look at the reducing the size of the sensor, for example design an SPR sensor while most of the sensing elements are on-a-chip. Another example is designing a fiber-based SPR sensor. Therefore, the size of the

sensing device can be reduced significantly and the device can be placed in small locations like pipelines for in-situ monitoring of asphaltene deposition and/or the effect of inhibitors on the asphaltene precipitants. Additionally, in-situ SPR is less sensitive to temperature and the components can be integrated using for example fiber optics. However, the temperature calibrations should be performed and fiber optic version of the SPR sensor instead of Kretschmann configuration should be developed. We can also use Kretschmann configuration and design pressure flanges.

4. As our SPR sensor is an effective phase change detector, we should also look at the different precipitants other than asphaltene in future projects.

5. Another interesting future direction is studying the variation in SPR peak and RI of the samples with temperature. Therefore, we can obtain the range of RI variation of crude oil or resin composite with increasing or decreasing the temperature.

6. We can also modify the theoretical model to perform sensitivity analysis with regard to penetration depth using a 2-layer approach, horizontally. For example, model crude oil could be used for 100 nm as a layer in the Matrix model (directly in contact with gold), with 1mm of n-heptane above it. This oil layer could be varied from 10 nm to 10,000 nm to determine sensitivity to penetration depth.

Bibliography

[1] M. B. Ritter, Y. Vlasov, J. A. Kash, and A. Benner, "Optical technologies for data communication in large parallel systems," *Journal of Instrumentation*, vol. 6, pp. C01012–C01012, Jan. 2011.

[2] D. White and J. Du Mont, "Visualizing sexual assault: An exploration of the use of optical technologies in the medico-legal context," *Social Science & Medicine*, vol. 68, pp. 1–8, Jan. 2009.

[3] M. Mehlmann and G. Gauglitz, "7 - surface spectroscopies," in *Surfaces and interfaces for biomaterials* (P. Vadgama, ed.), Woodhead Publishing Series in Biomaterials, pp. 183–199, Woodhead Publishing, Jan. 2005, ISBN: 978-1-85573-930-7.

[4] X. Yu, W. Zhang, P. Zhang, and Z. Su, "Fabrication technologies and sensing applications of graphene-based composite films: advances and challenges," *Biosensors and Bioelectronics*, vol. 89, pp. 72–84, Mar. 2017.

[5] M. Farré and D. Barceló, "Chapter 16 - sensor, biosensors and MIP based sensors," in *Food toxicants analysis* (Y. Picó, ed.), pp. 599–636, Amsterdam: Elsevier, Jan. 2007 , ISBN:978-0-444-52843-8.

[6] J. A. C. Heijmans, L. K. Cheng, and F. P. Wieringa, "Optical fiber sensors for medical applications — Practical engineering considerations," in *4th european conference of the international federation for medical and biological engineering* (J. Vander Sloten, P. Verdonck, M. Nyssen, and J. Haueisen, eds.), IFMBE Proceedings, (Berlin, Heidelberg), pp. 2330–2334, Springer, 2009, ISBN:978-3-540-89208-3.

[7] Y. Ruan, W. Yu, F. Cheng, X. Zhang, and S. Larré, "Detection of prostate stem cell antigen expression in human prostate cancer using quantum-dot-based technology," *Sensors*, vol. 12, pp. 5461–5470, May 2012.

[8] S. S. Mikhail, S. R. Schricker, S. S. Azer, W. A. Brantley, and W. M. Johnston, "Optical characteristics of contemporary dental composite resin materials," *Journal of Dentistry*, vol. 41, pp. 771–778, Sept. 2013.

[9] M. Machoy, J. Seeliger, L. Szyszka-Sommerfeld, R. Koprowski, T. Gedrange, and K. Woźniak, "The use of optical coherence tomography in dental diagnostics: a state-of-the-art review," *Journal of Healthcare Engineering*, vol. 2017, pp. 1–31, 2017.

[10] E. Benjumea, L. Díaz, C. Torres, E. Benjumea, L. Díaz, and C. Torres, "Tooth decay detection using a fiber optical sensor ," *Revista Facultad de Odontología Universidad de Antioquia*, vol. 29, June 2018.

[11] R. Khosravi, C. Rodriguez, F. Mostowfi, and V. Sieben, "Evaluation of crude oil asphaltene deposition inhibitors by surface plasmon resonance," *Fuel*, vol. 273, p. 117787, Aug. 2020.

[12] V. J. Sieben, S. Molla, F. Mostowfi, C. F. A. Floquet, A. Speck, and K. Chau, "Measuring asphaltene deposition onset from crude oils using surface plasmon resonance," *Energy & Fuels*, vol. 31, pp. 5891–5901, June 2017.

[13] P. K. Choudhury, "Optical sensors in environmental monitoring," *Current Science*, vol. 74, no. 9, pp. 723–725, 1998.

[14] Y. Takashima, M. Haraguchi, and Y. Naoi, "High-sensitivity refractive index sensor with normal incident geometry using a subwavelength grating operating near the ultraviolet wavelength," *Sensors and Actuators B: Chemical*, vol. 255, pp. 1711–1715, Feb. 2018.

[15] W. B. Ji, H. H. Liu, S. C. Tjin, K. K. Chow, and A. Lim, "Ultrahigh sensitivity refractive index sensor based on optical microfiber," *IEEE Photonics Technology Letters*, vol. 24, pp. 1872–1874, Oct. 2012.

[16] D. Liu, A. K. Mallik, J. Yuan, C. Yu, G. Farrell, Y. Semenova, and Q. Wu, "High sensitivity refractive index sensor based on a tapered small core single-mode fiber structure," *Optics Letters*, vol. 40, pp. 4166–4169, Sept. 2015.

[17] S. L. Pagliolico, V. R. L. Verso, A. Torta, M. Giraud, F. Canonico, and L. Ligi, "A preliminary study on light transmittance properties of translucent concrete panels with coarse waste glass inclusions," *Energy Procedia*, vol. 78, pp. 1811–1816, Nov. 2015.

[18] Z. Xiao, S. Yu, Y. Li, S. Ruan, L. B. Kong, Q. Huang, Z. Huang, K. Zhou, H. Su, Z. Yao, W. Que, Y. Liu, T. Zhang, J. Wang, P. Liu, D. Shen, M. Allix, J. Zhang, and D. Tang, "Materials development and potential applications of transparent ceramics: a review," *Materials Science and Engineering: R: Reports*, vol. 139, p. 100518, Jan. 2020.

[19] F. E. Nicodemus, "Directional reflectance and emissivity of an opaque surface," *Applied Optics*, vol. 4, pp. 767–775, July 1965.

[20] J. A. Lambert, "Forensic sciences— glass," in *Encyclopedia of analytical science (Second Edition)* (P. Worsfold, A. Townshend, and C. Poole, eds.), pp. 423–430, Oxford: Elsevier, Jan. 2005, ISBN: 978-0-12-816699-4.

[21] J. C. R. Reis, I. M. S. Lampreia, Â. F. S. Santos, M. L. C. J. Moita, and G. Douhéret, "Refractive index of liquid mixtures: theory and experiment," *ChemPhysChem*, vol. 11, pp. 3722–3733, Oct. 2010.

[22] M. Bass, C. DeCusatis, J. Enoch, V. Lakshminarayanan, G. Li, C. Macdonald, V. Mahajan, and E. Van Stryland, *Handbook of optics, third edition volume I: geometrical and physical optics, polarized light, components and instruments(set)*. USA: McGraw-Hill, Inc., third ed., 2009 , ISBN: 978-0-07-149889-0.

[23] F. Wooten, *Optical properties of solids*. Academic Press, oct 1972, ISBN: 978-0-12-763450-0.

[24] H. Fujiwara, *Spectroscopic ellipsometry: principles and applications*. John Wiley & Sons, sep 2007, ISBN: 978-0-470-06018-6.

[25] D. Gonçalves and E. A. Irene, "Fundamentals and applications of spectroscopic ellipsometry," *Química Nova*, vol. 25, pp. 794–800, Sept. 2002.

[26] H. G. Tompkins and E. A. Irene, "Handbook of ellipsometry,"

[27] Z. Bacsik, J. Mink, and G. Keresztury, "Ftir spectroscopy of the atmosphere. I. principles and methods," *Applied Spectroscopy Reviews*, vol. 39, pp. 295–363, Dec. 2004.

[28] C. Berthomieu and R. Hienerwadel, "Fourier transform infrared (FTIR) spectroscopy," *Photosynthesis Research*, vol. 101, pp. 157–170, Sept. 2009.

[29] P. Marsac, N. Piérard, L. Porot, W. Van den bergh, J. Grenfell, V. Mouillet, S. Pouget, J. Besamusca, F. Farcas, T. Gabet, and M. Hugener, "Potential and limits of FTIR methods for reclaimed asphalt characterisation," *Materials and Structures*, vol. 47, pp. 1273–1286, Aug. 2014.

[30] B. P. Jelle, T.-N. Nilsen, P. J. Hovde, and A. Gustavsen, "Accelerated climate aging of building materials and their characterization by fourier transform infrared radiation analysis," *Journal of Building Physics*, vol. 36, pp. 99–112, July 2012.

[31] N. Luan and J. Yao, "Refractive index and temperature sensing based on surface plasmon resonance and directional resonance coupling in a pcf," *IEEE Photonics Journal*, vol. 9, pp. 1–7, Apr. 2017.

[32] J. Homola, "Present and future of surface plasmon resonance biosensors," *Analytical and Bioanalytical Chemistry*, vol. 377, pp. 528–539, Oct. 2003.

[33] B. A. Prabowo, A. Purwidyantri, and K.-C. Liu, "Surface plasmon resonance optical sensor: a review on light source technology," *Biosensors*, vol. 8, Aug. 2018.

[34] H. Ahn, H. Song, J.-r. Choi, and K. Kim, "A localized surface plasmon resonance sensor using double-metal-complex nanostructures and a review of recent approaches," *Sensors (Basel, Switzerland)*, vol. 18, Dec. 2017.

[35] S. C. Sharma, "Surface plasmon resonance sensors: fundamental concepts, selected techniques, materials and applications," *Physical Sensors, Sensor Networks and Remote Sensing*, p. 54, July 2018.

[36] S. K. Raghuwanshi, M. Kumar, and B. S. Athokpam, "Analysis of novel class of surface plasmon phenomena having a metamaterial layer between two different metals for sensor application," *IEEE Sensors Journal*, vol. 16, pp. 6617–6624, Sept. 2016.

[37] R. B. M. Schasfoort, *Handbook of surface plasmon resonance: 2nd Edition*. Royal Society of Chemistry, May 2017, ISBN: 978-1-78262-730-2.

[38] J. Homola, S. S. Yee, and D. Myszka, "Chapter 4- surface plasmon resonance biosensors," in *Optical biosensors (Second Edition)* (F. S. Ligler and C. R. Taitt, eds.), 2008, ISBN: 978-0-444-53125-4.

[39] S. A. Maier, *Plasmonics: fundamentals and applications*. New York, NY: Springer US, 2007, ISBN: 978-0-387-33150-8 978-0-387-37825-1.

[40] A. B. Taylor and P. Zijlstra, "Single-molecule plasmon sensing: current status and future prospects," *ACS Sensors*, vol. 2, pp. 1103–1122, Aug. 2017.

[41] J. Homola and M. Piliarik, "Surface plasmon resonance (SPR) sensors," in *Surface plasmon resonance based sensors* (J. Homola, ed.), vol. 4, pp. 45–67, Berlin, Heidelberg: Springer Berlin Heidelberg, 2006, ISBN: 0009-2665, 1520-6890.

[42] J. Wang, W. Lin, E. Cao, X. Xu, W. Liang, and X. Zhang, "Surface plasmon resonance sensors on raman and fluorescence spectroscopy," *Sensors*, vol. 17, p. 2719, Nov. 2017.

[43] J. Homely and M. Piliarik, "Surface plasmon resonance (SPR) sensors," in *Surface plasmon resonance based sensors* (J. Homola, ed.), vol. 4, pp. 45–67, Berlin, Heidelberg: Springer Berlin Heidelberg, 2006, ISBN: 978-3-540-33918-2 978-3-540-33919-9.

[44] K. Kurihara and K. Suzuki, "Theoretical understanding of an absorption-based surface plasmon resonance sensor based on Kretchmann's theory," *Analytical Chemistry*, vol. 74, pp. 696–701, feb 2002.

[45] M. J. Weber, *Handbook of optical materials*. The CRC Press Laser and Optical Science and Technology Series, Boca Raton: CRC Press, 2003, ISBN: 978-0-8493-3512-9.

[46] P. B. Johnson and R. W. Christy, "Optical constants of the noble metals," *Physical Review B*, vol. 6, pp. 4370–4379, Dec. 1972.

[47] A. D. Rakić, A. B. Djurišić, J. M. Elazar, and M. L. Majewski, "Optical properties of metallic films for vertical-cavity optoelectronic devices," *Applied Optics*, vol. 37, pp. 5271–5283, Aug. 1998.

[48] V. J. Sieben, A. J. Stickel, C. Obiosa-Maife, J. Rowbotham, A. Memon, N. Hamed, J. Ratulowski, and F. Mostowfi, "Optical measurement of saturates, aromatics, resins, and asphaltenes in crude oil," *Energy & Fuels*, vol. 31, pp. 3684–3697, Apr. 2017.

[49] M. H. Schneider, V. J. Sieben, A. M. Kharrat, and F. Mostowfi, "Measurement of asphaltenes using optical spectroscopy on a microfluidic platform," *Analytical Chemistry*, vol. 85, pp. 5153–5160, May 2013.

[50] O. C. Mullins, E. Y. Sheu, A. Hammami, and A. G. Marshall, "Asphaltenes, heavy oils, and petroleomics," Springer, Nov. 2007, ISBN: 978-0-387-68903-6.

[51] J. Wang, J. S. Buckley, and J. L. Creek, "Asphaltene deposition on metallic surfaces," *Journal of Dispersion Science and Technology*, vol. 25, pp. 287–298, Dec. 2004.

[52] M. M. Shadman, A. H. S. Dehaghani, M. V. Sefti, and M. Dehghanizadeh, "The effect of inhibitors on asphaltene precipitation in crude oil using the viscometric method," *Energy Sources, Part A: Recovery, Utilization, and Environmental Effects*, vol. 34, pp. 827–838, Feb. 2012.

[53] A. C. S. Ramos, *Asphaltene petroleum brazilian: aggregation in aromatic solvents and additives stabilization in emulsions*. PhD Thesis, Ph. D. thesis Campinas,, Brazil: University of Estadual, 2001.

[54] M. Zoveidavianpoor, A. Samsuri, and S. R. Shadizadeh, "The clean up of asphaltene deposits in oil wwells," *Energy Sources, Part A: Recovery, Utilization, and Environmental Effects*, vol. 35, pp. 22–31, Jan. 2013.

[55] S. C. R. Verdier, *Experimental study and modelling of asphaltene precipitation caused by gas injection*. PhD Thesis, Technical University of Denmark, Sept. 2006, ISBN: 978-87-91435-42-3.

[56] R. J. Dyer, "Method for simultaneous removal of asphaltene, and/or paraffin and scale from producing oil wells," Mar. 2010, number = US7670993B2.

[57] G. Zahedi, A. R. Fazlali, S. M. Hosseini, G. R. Pazuki, and L. Sheikhattar, "Prediction of asphaltene precipitation in crude oil," *Journal of Petroleum Science and Engineering*, vol. 68, pp. 218–222, Oct. 2009.

[58] M. Madhi, R. Kharrat, and T. Hamoule, "Screening of inhibitors for remediation of asphaltene deposits: Experimental and modeling study," *Petroleum*, vol. 4, pp. 168–177, June 2018.

[59] T. Lu, Z. Li, W. Fan, X. Zhang, and Q. Lv, "Nanoparticles for inhibition of asphaltenes deposition during CO2 flooding," *Industrial & Engineering Chemistry Research*, vol. 55, pp. 6723–6733, June 2016.

[60] A. Khormali, "Asphaltene precipitation and inhibition in carbonate reservoirs," *Petroleum Science and Technology*, vol. 35, pp. 515–521, Mar. 2017.

[61] F. Salimi, J. Salimi, and M. Abdollahifar, "Investigation of asphaltene deposition under dynamic flow conditions," *Petroleum Science*, vol. 13, pp. 340–346, May 2016.

[62] J. C. Franco, G. Gonçalves, M. S. Souza, S. B. C. Rosa, L. M. Thiegue, T. D. Z. Atvars, P. T. V. Rosa, and R. A. Nome, "Towards in situ fluorescence spectroscopy and microscopy investigations of asphaltene precipitation kinetics," *Optics Express*, vol. 21, pp. 30874–30885, Dec. 2013.

[63] A. G. Ryder, "Time-resolved fluorescence spectroscopic study of crude petroleum oils: influence of chemical composition:," *Applied Spectroscopy*, vol. 58, pp. 613–623, Aug. 2016.

[64] Y. G. Burya, I. K. Yudin, V. A. Dechabo, V. I. Kosov, and M. A. Anisimov, "Light-scattering study of petroleum asphaltene aggregation," *Applied Optics*, vol. 40, pp. 4028–4035, Aug. 2001.

[65] P. Wattana, D. J. Wojciechowski, G. Bolaños, and H. S. Fogler, "Study of asphaltene precipitation using refractive index measurement," *Petroleum Science and Technology*, vol. 21, pp. 591–613, Jan. 2003.

[66] A. Sivaraman, Y. Hu, F. Thomas, D. Bennion, and A. Jamaluddin, "Acoustic resonance: An emerging technology to identify wax and asphaltene precipitation onset conditions in reservoir fluids," *Pet Soc Canada*, pp. 97–196, 1997.

[67] F. M. Vargas and M. Tavakkoli, *Asphaltene deposition: fundamentals, prediction, prevention, and remediation*. CRC Press, Taylor and Francis, May 2018, ISBN: 978-1-351-97731-9.

[68] M. Milanese, A. Ricciardi, M. G. Manera, A. Colombelli, G. Montagna, A. de Risi, and R. Rella, "Real time oil control by surface plasmon resonance transduction methodology," *Sensors and Actuators A: Physical*, vol. 223, pp. 97–104, Mar. 2015.

[69] M. D. Ooms, H. Fadaei, and D. Sinton, "Surface plasmon resonance for crude oil characterization," *Energy & Fuels*, vol. 29, pp. 3019–3023, May 2015.

[70] A. Yen, Y. R. Yin, and S. Asomaning, "Evaluating asphaltene inhibitors: laboratory tests and field studies," in *SPE international symposium on oil field chemistry*, Society of Petroleum Engineers, Jan. 2001, ISBN: 978-1-55563-924-2.

[71] L. Kai-Qun, W. Lai-Ming, Z. Dou-Guo, Z. Rong-Sheng, W. Pei, L. Yong-Hua, and M. Hai, "Temperature effects on prism-based surface plasmon resonance sensor," *Chinese Physics Letters*, vol. 24, pp. 3081–3084, Oct. 2007.

[72] A. K. George and R. N. Singh, "Correlation of refractive index and density of crude oil and liquid hydrocarbon," *International Journal of Chemical, Environmental Biological Sciences (IJCEBS)*, vol. 3, no. 5, p. 3, 2015.

[73] T. Maqbool, P. Srikiratiwong, and H. S. Fogler, "Effect of temperature on the precipitation kinetics of asphaltenes," *Energy & Fuels*, vol. 25, pp. 694–700, Feb. 2011.

[74] A. Santini, I. T. Gallegos, and C. M. Felix, "Photoinitiators in dentistry: A Review," *Primary Dental Journal*, vol. 2, pp. 30–33, Oct. 2013.

[75] M. Fornabaio, H. Reveron, E. Adolfsson, L. Montanaro, J. Chevalier, and P. Palmero, "Design and development of dental ceramics: examples of current innovations and future concepts," in *Advances in Ceramic Biomaterials* (P. Palmero, F. Cambier, and E. De Barra, eds.), pp. 355–389, Woodhead Publishing, Jan. 2017, ISBN: 978-0-08-100881-2.

[76] A.-H. Eom, D.-S. Kim, S.-H. Lee, C.-W. Byun, N.-H. Park, and K.-K. Choi, "Optical characteristics of resin composite before and after polymerization," *Journal of Korean Academy of Conservative Dentistry*, vol. 36, no. 3, p. 219, 2011.

[77] J. L. Ferracane, "Resin composite state of the art," *Dental Materials*, vol. 27, pp. 29–38, Jan. 2011.

[78] J. Homola, "Surface plasmon resonance sensors for detection of chemical and biological species," *Chemical Reviews*, vol. 108, pp. 462–493, Feb. 2008.

[79] D20 Committee, "Test method for rockwell hardness of plastics and electrical insulating materials," tech. rep., ASTM International.

Appendix A

Copyright permissions

[September 15, 2020]

Dear Ms. Raha khosravi,

Thank you for your email.

Please note that, as one of the Authors of this article, you retain the right to reuse it in your thesis/dissertation. You do not require formal permission to do so.

You are permitted to post this Elsevier article online if it is embedded within your thesis. Suitable acknowledgement to the source must be made, either as a footnote or in a reference list at the end of your publication.

You are also permitted to post your Author Accepted Manuscript online. However posting of the final published article is prohibited. "As per our Sharing Policy, authors are permitted to post the Accepted version of their article on their institutional repository – as long as it is for internal institutional use only. It can only be shared publicly on that site once the journal-specific embargo period has lapsed. For a list of embargo periods please see: https://www.elsevier.com You are not permitted to post the Published Journal Article (PJA) on the repository." Please feel free to contact me if you have any queries. Kind regards Anita Anita Mercy Senior Copyrights Coordinator – Copyrights Team Elsevier — Health Content Operations (A division of Reed Elsevier India Pvt. Ltd.) Ascendas International Tech Park, Crest - 12th Floor—Taramani, Chennai 600113 • India— Tel: +91 4442994696